

Electronic Thesis and Dissertation Repository

7-28-2015 12:00 AM

Evaluation of Radiation Dose-Response in a Breast Cancer Brain Metastasis Model

Niloufar Zarghami
The University of Western Ontario

Supervisor
Dr. Eugene Wong
The University of Western Ontario

Graduate Program in Medical Biophysics
A thesis submitted in partial fulfillment of the requirements for the degree in Master of Science
© Niloufar Zarghami 2015

Follow this and additional works at: <https://ir.lib.uwo.ca/etd>



Part of the [Medical Biophysics Commons](#)

Recommended Citation

Zarghami, Niloufar, "Evaluation of Radiation Dose-Response in a Breast Cancer Brain Metastasis Model" (2015). *Electronic Thesis and Dissertation Repository*. 3028.
<https://ir.lib.uwo.ca/etd/3028>

This Dissertation/Thesis is brought to you for free and open access by Scholarship@Western. It has been accepted for inclusion in Electronic Thesis and Dissertation Repository by an authorized administrator of Scholarship@Western. For more information, please contact wlsadmin@uwo.ca.

Evaluation of Radiation Dose-Response in a Breast Cancer Brain Metastasis Model

(Thesis format: Integrated Article)

by

Niloufar Zarghami

Graduate Program in Medical Biophysics

A thesis submitted in partial fulfillment
of the requirements for the degree of
Master of Science

The School of Graduate and Postdoctoral Studies
The University of Western Ontario
London, Ontario, Canada

© Niloufar Zarghami 2015

Abstract

The second incidence of brain metastases is from breast cancer. Radiotherapy, a standard treatment for brain metastasis, limits cancer division by inducing DNA double-stranded breaks (DSBs). Currently, identical radiation doses are prescribed for all types of brain metastases but little is known about their histological responses. In this thesis, we initiated a radiation dose-response study in a triple-negative human breast cancer brain metastasis mouse model using a custom designed 3D-printed restrainer to assist half-brain irradiation. We quantified the amount of DSBs in tumors and mouse brain tissues using γ -H2AX marker at 30 minutes (acute) and 11 days (longitudinal) after treatment with doses of 8-24 Gy. We also evaluated tumors' response using histology and MRI. In the longitudinal study we found significant differences in the amount of DSBs, tumor cell density, and nucleus size between irradiated surviving and non-irradiated tumors. These results gave insights to brain metastasis response after radiotherapy.

Keywords

Breast cancer brain metastasis, Small animal radiation therapy, Radiation dose-response, Radiation biology, DNA double-strand breaks, γ -H2AX, Mouse head holder, 3D-printing technology, Preclinical MRI

Co-Authorship Statement

The following thesis contains one manuscript that has been submitted for publication and one in preparation to be submitted to the peer-reviewed scientific journal.

Chapter 2 encompasses the original manuscript submitted to the *Journal of Medical Physics* entitled “Immunohistochemical evaluation of mouse brain irradiation targeting accuracy with 3D-printed immobilization device”. The manuscript was co-authored by Niloufar Zarghami, Michael Jensen, Srikanth Talluri, Paula Foster, Ann Chambers, Fred Dick and Eugene Wong. As the 1st author, I assisted with modeling and design of the head holder, conducting animal experiments, data acquisition, analysis and writing the manuscript. Michael Jensen provided advice regarding the design of the head holder and irradiation procedure. Srikanth Talluri helped with the histology and immunohistochemistry. Drs. Paula Foster, Ann Chambers and Fred Dick provided feedback for the manuscript. Dr. Eugene Wong helped determine research objectives, provided mentorship, supervision, and editorial assistance.

Chapter 3 contains basis of an original manuscript in preparation to be submitted to the *International Journal of Radiation Oncology * Biology * Physics* entitled “Evaluation of radiation-induced DNA double-stranded breaks and tumor response in a breast cancer brain metastases model”. The co-authors of this manuscript are Niloufar Zarghami, Donna Murrell, Michael Jensen, Fred Dick, Ann Chambers, Paula Foster and Eugene Wong. I was responsible for the design of the study, analysis, interpretation and writing of the manuscript. Donna Murrell assisted with cell culture, MRI scans and imaging data acquisition. Michael Jensen helped with the irradiation, dosimetry, and histological quantification. Carmen Simeirea assisted with mouse intra-cardiac injection. Drs. Ann Chambers, Paula Foster, and Fred Dick provided advice regarding the study design and presentation of data. Dr. Eugene Wong assisted with experimental design, provided mentorship, supervision, and editorial assistance.

Acknowledgments

First and foremost, I would like to express my deepest appreciation to my supervisor Dr. Eugene Wong, who has inspired me to think beyond boundaries. I am very grateful to him for challenging me and pushing me much further than I thought possible. Through his leadership and guidance, I was motivated and excited to create and develop this thesis. I would like to thank Dr. Wong for the opportunity he has given me, the ample amount of support he provided and the doors he has opened for my future.

I would like to thank the members of my committee, Drs. Paula Foster and Ann Chambers for providing me with guidance and support. I am very grateful for their insightful comments and expertise. I would also like to thank Dr. Fred Dick for providing me the opportunity to pursue my research in the field of cancer biology; an area that I am passionate about and has provided me an unparalleled learning experience.

I would like to extend a massive thank you to members of Wong lab. I truly appreciated and enjoyed all of our group meetings and discussions. To Dr. Jeff Chen- I am most fortunate to have you in our meetings. You are an ultimate role model of medical physicist/scientist. To Michael Jensen- thank you for your leadership and support. You were always there to guide me. To Tom Hrinivich and Anthony Lausch- thank you for helping me with statistics and coding.

I am very grateful to our entire collaborator for this thesis. From Foster lab: Donna Murrell- thanks for all those early morning and late night scans and our incredible discussions. To Yuhua Chen and Carmen Simeirea - this project would not be possible without the help of you, thanks for teaching me perfusion and mouse surgery. I would like to acknowledge the members of Dick lab, Srikanth, Daniel, James, Piru and Charles for helping me with staining and creating a welcoming environment and Jean-Guy Belliveau for helping with 9.4T scanner.

Most importantly, I would like to thank those closest to me. To my grandmother, mother, father and brother. Thank you for all your support, courage and unconditional love. You taught me the importance of perseverance, commitment, and academic inquisitiveness. My friends, Nastaran, Shahrzad, and Shamin - my life is filled with joy because of you! To Farhang-for your unconditional support and encouragement throughout my degree.

Finally, I am thankful for the financial support I have received during my graduate studies that allowed me to focus my time and energy on research. I acknowledge funding support from the Ontario Graduate Scholarship and the Pamela Greenaway-Kohlmeier Translational Breast Cancer Research Unit.

Table of Contents

Abstract	ii
Co-Authorship Statement.....	iii
Acknowledgments	iv
List of Tables.....	ix
List of Figures.....	x
List of Abbreviations	xii
List of Appendices.....	xiv
Chapter 1.....	1
1 General Introduction.....	1
1.1 Cancer.....	1
1.1.1 Breast Cancer	1
1.1.2 Triple-Negative Breast Cancer Subtype	3
1.1.3 Metastasis	4
1.1.4 Breast Cancer Metastasis.....	8
1.1.5 Breast Cancer Brain Metastases Preclinical Models	10
1.2 Radiation Therapy	11
1.2.1 Radiobiology Principles	11
1.2.2 DNA Double-Stranded Breaks (DSBs).....	12
1.2.3 Radiation Therapy Dose-Response Relationship.....	15
1.2.4 Preclinical Radiation Therapy Devices.....	16
1.3 Magnetic Resonance Imaging (MRI).....	17
1.3.1 Balanced Steady State Free Precession (bSSFP) MRI Sequence.....	18
1.4 Three-Dimensional (3D) Printing Technology.....	19
1.5 Thesis Objectives and Outline	20
1.6 References.....	22

Chapter 2	32
2 Immunohistochemical Evaluation of Mouse Brain Irradiation Targeting Accuracy with 3D-Printed Immobilization Device.....	32
2.1 Introduction.....	32
2.2 Methods and Materials	33
2.2.1 Head Holder Design and 3D-Printing	33
2.2.2 Mouse Brain Irradiation	35
2.2.3 Immunohistochemistry	37
2.2.4 Analysis	38
2.3 Results	39
2.3.1 Mouse Set-up in 3D-printed Head Holder.....	39
2.3.2 Validating Beam Targeting Accuracy with γ -H2AX Staining	39
2.4 Discussion	41
2.5 Conclusions.....	42
2.6 Acknowledgment.....	42
2.7 References.....	43
Chapter 3	45
3 Evaluation of Radiation-Induced DNA Double-Stranded Breaks and Tumor Response in a Breast Cancer Brain Metastasis Model.....	45
3.1 Introduction.....	45
3.2 Material and Methods.....	47
3.2.1 Cell Culture.....	47
3.2.2 Animal Model.....	48
3.2.3 <i>In-Vivo</i> MRI.....	49
3.2.4 Mouse Hemi-Brain Irradiation	49
3.2.5 Immunohistochemistry	51
3.2.6 Histological Quantification.....	53
3.2.7 MRI Analysis	56
3.2.8 Statistics	56

3.3	Results	56
3.3.1	γ -H2AX Radiation Dose-response.....	56
3.3.2	Tumor Cell Nuclear Size	62
3.3.3	Tumor Cell Density	64
3.3.4	<i>In-vivo</i> Dose-Response	66
3.4	Discussion	69
3.5	Conclusions.....	72
3.6	Acknowledgment.....	72
3.7	References.....	73
Chapter 4.....		80
4	Conclusions and Future Directions.....	80
4.1	Chapter 2	80
4.1.1	3D-Printed Mouse Holder: Summary	80
4.1.2	Future Work	81
4.2	Chapter 3	81
4.2.1	Acute Radiation Dose-Response Study: Summary	81
4.2.2	Acute Radiation Dose-Response Study: Future Work.....	82
4.2.3	<i>Ex-Vivo</i> Longitudinal Radiation Dose-Response Study: Summary.....	82
4.2.4	<i>Ex-Vivo</i> Longitudinal Radiation Dose-Response Study: Future Work.....	83
4.2.5	<i>In-Vivo</i> Longitudinal Radiation Dose-Response Study: Summary	83
4.2.6	<i>In-Vivo</i> Longitudinal Radiation Dose-Response Study: Future work.....	84
4.3	References.....	85
Appendices		87
Appendix A: Animal Use Protocol.....		87
Appendix B: Fluorescent γ -H2AX Immunohistochemistry Standard Operating Procedure....		88
Appendix C: License and Permission Usage.....		89
Curriculum Vitae.....		90

List of Tables

Table 1-1: Breast cancer classification based on histopathological markers.	3
Table 2-1: Targeting accuracy measurement of γ -H2AX stained brain sections..	40
Table 3-1: Irradiation group schedule for acute and longitudinal study.....	48

List of Figures

Figure 1-1: Schematic of the metastasis process.....	5
Figure 1-2: Main sites of metastasis in breast cancer patients and their incidencep	9
Figure 1-3: Image of mouse brain tissue 30 minutes after receiving ~1 Gy, stained with fluorescent anti- γ -H2AX antibody.....	13
Figure 1-4: DNA is wrapped around core histone proteins. Upon DNA double-strand break, one of the histone proteins, H2AX, gets rapidly phosphorylated by ATM adjacent to the site of damage. The phosphorylated H2AX is termed γ -H2AX.....	15
Figure 1-5: Processes involved in 3D-printing.....	20
Figure 2-1: 3D-printed mouse head holder.....	35
Figure 2-2: Pre-treatment CT images of the mouse brain positioned in 3D-printed head holder.....	36
Figure 2-3: Beam's eye view fluoroscopy image of the mouse from the top (dorsal-ventral view).....	37
Figure 2-4: Fluorescence microscopy of γ -H2AX stained brain sections (red), imaged at 10X magnification.....	39
Figure 3-1: Radiation dose-response experimental design.....	50
Figure 3-2: Calculated dose distribution on coronal CT plane of the mouse brain.....	51
Figure 3-4: Flow chart of the processes involved in the quantification of γ -H2AX intensity, tumor nucleus size and tumor cell density.....	55
Figure 3-5: Whole brain image of γ -H2AX stained brain section (red), imaged at 10X.....	57
Figure 3-6: Initial DNA damage response 30 minutes post-irradiation.....	58

Figure 3-7: Quantification of the intensity of γ -H2AX staining versus radiation dose 30 minutes after radiotherapy.	59
Figure 3-8: Residual DNA damage response 11 days post-irradiation.....	60
Figure 3-9: Quantification of the intensity of γ -H2AX staining for the various radiation dose 11 days after radiotherapy.....	61
Figure 3-10: DAPI staining of tumor nuclei 11 days after radiotherapy.	62
Figure 3-11: Average size of tumor nuclei 30 minutes after radiotherapy.	63
Figure 3-12: Average size of tumor nuclei 11 days after radiotherapy.	63
Figure 3-13: H&E stained sections of tumors 11 days after radiotherapy.....	64
Figure 3-14: The tumor cell density 30 minutes after radiotherapy.	65
Figure 3-15: The tumor cell density 11 days after radiotherapy.....	66
Figure 3-16: MR images (bSSFP) of the mouse brain at two-time points.....	67
Figure 3-17: The mean fractional growth of brain metastases measured on MR images for various radiation doses.....	68
Figure 4-1: Mouse brain tumor model imaged with DWI sequence on 9.4T scanner.....	84

List of Abbreviations

3D	Three-dimensional
53PB1	TP53 binding protein 1
ACVS	Animal care and veterinary services
ADC	Apparent diffusion coefficient
ANOVA	Analysis of variance
ATM	Ataxia telangiectasia mutated
ATR	ATM-and Rad3-related
BED	Biological effective dose
BB	Ball bearing
BBB	Blood-brain barrier
BCBM	Breast cancer brain metastasis
BM	Brain metastasis
bSSFP	Balanced steady-state free precession
CAD	Computer aided design
CBCT	Cone beam computed tomography
CNS	Central nervous system
CT	Computed tomography
DAPI	4', 6-diamidino-2-phenylindole
DDR	DNA damage response
DMEM	Dulbecco's modified eagle's medium
DNA	Deoxyribonucleic Acid
DNA-PKcs	DNA-dependent protein kinase catalytic subunit
DSB	Double strand break
DWI	Diffusion weighted imaging
EGFP	Enhanced green fluorescent protein
ER	Estrogen receptor
Gd	Gadolinium
H&E	Hematoxylin and Eosin

HER2	Human growth factor receptor 2
IC	Intra-cardiac
IgG	Immunoglobulin G
IHC	Immunohistochemistry
IR	Ionizing radiation
IRIF	Ionizing radiation-induced foci
KPS	Karnofsky performance status
LF	Longitudinal fissure
MRI	Magnetic resonance imaging
PFA	Paraformaldehyde
PFGE	Pulsed field electrophoresis
PIKK	Phosphoinositide 3-kinase-related-kinase
PR	Progesteron receptor
RT	Radiation therapy
SRS	Stereotactic radiosurgery
STL	Stereolithography
T	Tesla
TE	Echo time
TNBC	Triple-negative breast cancer
TR	Repetition time
WBRT	Whole brain radiation therapy

List of Appendices

Appendix A: Animal Use Protocol.....	87
Appendix B: Fluorescent γ -H2AX Immunohistochemistry Standard Operating Procedure on Mouse Frozen Sections.....	88
Appendix C: License and Permission Usage.....	89

Chapter 1

1 General Introduction

Cancer is one of the most severe and potentially life-threatening diseases. The high morbidity and mortality rate is primarily due to the progression to the metastatic stage. Radiation therapy has been, and continues to be, an important treatment modality for patients diagnosed with cancer. This is especially true in the treatment of brain metastases because of limited drug penetration through the blood brain barrier, or tumors become refractory after multiple lines of chemotherapies, or appear in locations that are inoperable, leaving radiation therapy the only management option. Mechanisms of tumor response/resistance to radiation therapy remain unclear. With the advent of new biological markers, tumor models and novel imaging techniques, we revisit these radiobiological challenges in the preclinical setting. This introductory chapter provides an overview of breast cancer and brain metastasis from this origin, treatment options, principles of radiobiology as well as techniques for quantifying radiation damage, preclinical radiation therapy and imaging technique used in this thesis.

1.1 Cancer

1.1.1 Breast Cancer

Breast cancer is the most common malignancy among both American and Canadian women.^[1,2] It is estimated in 2015, 231,840 women in the USA and 25,000 in Canada will be diagnosed with breast cancer.^[2,3] Breast cancer also has the second highest mortality rate after lung and bronchus cancer in women. This cancer has a low incidence in men and accounts for less than 1% of all breast cancer cases.^[2,3]

Breast cancer is a heterogeneous disease. There is diversity in breast cancer morphology and characteristics, response to treatment and patient's clinical outcome. The high degree of heterogeneity can be seen in breast cancer structure, pathological features and even

within an individual tumor.^[4] Breast cancer can be segregated into three groups based on its structure and origin:

- 1) Invasive ductal carcinoma, 75% of cases,
- 2) Invasive lobular carcinoma, ~15% of cases, and
- 3) Other types such as medullary, neuroendocrine, tubular, apocrine, metaplastic, adenoid cystic and micropapillary, ~10% of cases.^[4,5]

Another approach to classify breast cancer is by their histopathological characteristics. Based on the status of hormone receptors such as estrogen (ER) and progesterone (PR), overexpression of the human epidermal growth factor receptor 2 (HER2) oncogene and Ki-67 labeling index, a proliferation marker, breast cancer has been classified to four major subtypes.^[6,7] Although there are other classifiers for breast cancer, histopathological markers are known to be widely adopted in the clinics.^[4,8,9] Table 1-1 shows breast cancer subtypes based on their molecular markers and their prevalence. Other subtypes of breast cancer such as normal like, apocrine molecular type and claudin-low type, are less frequent.

The status of the receptors is a critical predictor of both treatment decision and patient prognosis. Subtypes that express receptors on their surface are known to be suitable candidates for hormonal and targeted therapy. For example, Trastuzumab (Herceptin) is a monoclonal antibody that is currently used as an adjuvant treatment in early stage HER2 positive patients.^[10] On the other hand, subtypes such as triple-negative do not have a well-defined therapy targets.^[4]

Table 1-1: Breast cancer classification based on histopathological markers^[6,8]

Breast cancer subtype	Approximate prevalence	Marker expression status
Luminal-A	50-60%	HER2 negative, ER and/or PR positive, Ki-67 low
Luminal-B	15%-20%	HER2 negative, ER positive, either Ki-67 high or PR low HER2 positive, ER positive, any Ki-67, any PR
HER2 overexpression	15-20%	HER2 positive and amplified, ER and PR negative
Triple - negative	15-25%	HER2 negative, ER and PR negative

1.1.2 Triple-Negative Breast Cancer Subtype

The triple-negative breast cancer (TNBC) subtype is defined by the absence of hormone receptors (ER, PR) and lack of HER2 expression on immunohistochemical (IHC) analysis in the clinical setting.^[6] In this thesis, we employed a TNBC cell line for our radiation dose-response study. Most of the TNBC cells have a ductal origin (90.7%) and are poorly differentiated.^[11] This breast cancer subtype occurs more in young women, with African or Hispanic ancestry.^[12] Triple-negative breast cancer usually associated with poor prognosis and aggressive clinicopathological features.^[13] Less than 30% of triple-negative patients survive more than 5 years.^[12] TNBC has also a distinct

recurrence pattern. Patients diagnosed with triple-negative breast cancer are frequently young and recurrence occurs 3 to 5 years after initial diagnosis. The incidence of late recurrence (more than 5 years) in these patients is lower compared to other breast cancer subtypes.^[11] The treatment of triple-negative cells remains challenging. The primary reason is, this subtype does not express ER/PR and HER2 receptors on the cell surface which limits the use of endocrinal therapy or available targeted drugs.^[12] Breast-conserving surgery followed by radiation therapy and/or cytotoxic chemotherapy are the common treatment options for these patients.

1.1.3 Metastasis

Frequently, it is not the primary cancer that a patient succumbs to, but what makes cancer a life-threatening disease is when it gains the ability to escape from the primary site and spread to other organs. This process is known as metastasis.^[14] Most of the tumors select either lymphatic or hematogenous (blood-stream) routes to leave the primary organ.^[15] However, when these cells are in the circulatory system, the pattern and the micro-environmental conditions in the host organs play a crucial role in the ultimate fate of the primary tumor cells.^[16-18] Metastasis is an inefficient process, and usually less than 0.01% circulating tumor cells can complete all the steps shown in Figure 1-1 and form metastasis^[15,17,19]; thus this tiny subset is responsible for the majority of cancer deaths. As we will be using a preclinical brain metastasis model in this thesis, we will focus on brain metastasis next.

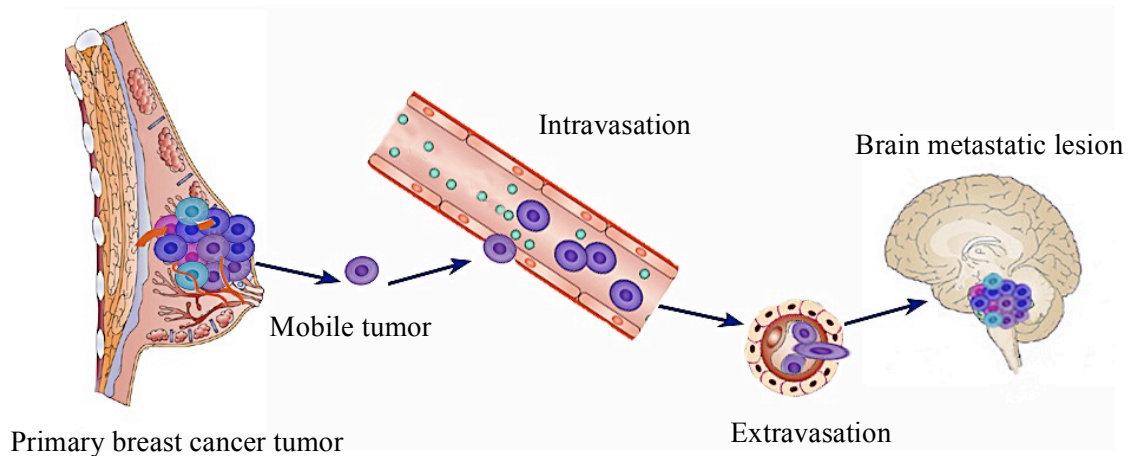


Figure 1-1: Schematic of the metastasis process. The metastatic cascade consists of multiple steps that the primary tumor cells have to take in order to travel and grow in the secondary site. Adapted from reference 19.

1.1.3.1 Brain Metastasis

Brain metastasis occurs when the primary tumor cells escape from their origin via arterial circulation, extravasate across the capillary membrane of brain parenchyma and finally seed and grow efficiently in the brain.^[18] It is known that brain metastasis is the primary reason for morbidity and mortality with 8.1% overall survival at two years.^[20] Brain metastases occur approximately in 20-40% adult patients with systemic malignancies and the incidence is up to 10 times higher than primary malignant brain tumors.^[18,21,22] In the USA, it is expected that 21,651 to 43,301 new cases of brain metastasis from any primary origin be diagnosed each year.^[20] Nonetheless, the incidence and prevalence of brain metastasis is rising.^[22] The primary reason is prolonged survival due to improved treatment outcomes of primary cancer. Some of monoclonal antibody drugs such as Trastuzumab (Herceptin), which are effective for treating systemic malignancies, cannot penetrate to the brain.^[18,20] Moreover, advances in noninvasive screening tools and modalities such as magnetic resonance imaging (MRI), have contributed in detection of brain metastasis lesions.

Breast cancer (20-30%) is the second most common source of brain metastases. Other primary malignancies responsible for brain metastasis include: Lung cancer (40-50%), melanoma (5-10%), lymphoma and other sites (4-6%).^[18,23]

1.1.3.2 Brain Metastases Management

The treatment of patients diagnosed with brain metastasis remains clinically challenging due to unique features of the brain. Un-treated brain metastasis causes increased intracranial pressure, which results in median survival of only one month.^[21,24] The main treatment options for brain metastasis are surgery, radiation therapy (RT), stereotactic radiosurgery (SRS) and corticosteroids (e.g. Dexamethasone). Chemotherapy is not routinely used as the primary treatment modality for patients diagnosed with brain metastasis.^[21] Most of the treatments for these patients are considered to improve the quality of life and achieve neurological palliation. The optimal selection of treatment combination for brain metastasis relies on factors such as the anatomical location of the lesion, number and size of the brain metastases, patient's age, performance status, extent of extracerebral tumor burden and histological features.^[24]

Surgery is the treatment of choice if stringent conditions are satisfied. Surgery can be performed only on accessible sites and depends on the general condition of the patient, number and size of the metastasis.^[20,21] Advances in neuro-oncology techniques have enabled surgeons to resect both single and multiple lesions (2-4) with reduced risks of post-operative complications.^[24]

Radiation therapy (RT) is the most commonly used treatment modality for patients diagnosed with brain metastases since the 1970s. The primary reason for this is almost 50% of these patients have at least three metastases at the time of the diagnosis ruling out surgery. Whole brain radiation therapy (WBRT) is valued for addressing both macro and micrometastasis. Moreover, WBRT is an integral part of the adjuvant treatment for patients with brain metastases following surgery.^[24,25] WBRT is a common fractionated external RT technique, in which the whole skull of the patients receives

uniform radiation dose while sparing the eyes. The radiation absorbed in the tissue is often represented as deposited energy per unit mass ($[J/Kg]=Gy$).^[26] The most common radiation dose/fractionation scheme for WBRT is 30 Gy delivered in 10 fractions over two weeks. There is no agreement on the optimum radiation dose schedule/fractionation, and the majority of clinical trials could not provide sufficient evidence of alternative dosing schedules.^[25,27] Acute radiation side effects such as alopecia (hair loss), dry desquamation (skin peeling), excessive fatigue and transient neurological symptoms can be seen in patients that receive WBRT. However, using steroids during RT may help with these symptoms. Generally long-term and chronic RT complications in these patients are not seen^[27,28] as the median survival of patients treated with WBRT alone is estimated to be 7 months,^[20] but it has been reported that the response to the WBRT is related to the primary histology of brain metastasis.^[25]

Stereotactic Radiosurgery (SRS) is another RT method, which employs collimated beams usually delivered in an arc around the tumor in a single or a small number of fractions. Unlike WBRT technique, SRS delivers the radiation toward a lesion identified on CT or MRI and spare the normal brain tissues by spreading low doses to a large volume. It is a minimally invasive procedure and associated with high local control rates (80-98% range).^[24,28] Depending on the size of the tumor, radiation dose varies between 18-24 Gy in one fraction. SRS is a better treatment option for preserving neurocognitive function. However, SRS as the sole treatment has been advocated for patients with small lesions (maximum size < 3 cm) and with 3 or fewer metastases in their brain.^[21,25,29] The overall survival of patients treated only with SRS has been reported to be 7.5-12.5 months.^[24]

WBRT is often used in combination with SRS. Retrospective studies have shown that the combination of these two modalities may improve the overall survival in patients diagnosed with brain metastases in the absence of extra-cranial progression.^[24]

Chemotherapy is usually the last option for brain metastases patients. It is often prescribed when the patient cannot undergo surgery and/or RT. Chemotherapy drugs can also be used in combination with other treatments to suppress extracranial malignancies.

One of the unique hurdles of treating tumors in the brain is the blood-brain barrier (BBB). The tight junctions between brain endothelial cells control the passage of substrates from the blood into the brain parenchyma. Thus, the penetration of the chemotherapeutic drugs to the brain and their efficacy depend on their solubility, size and molecular structure.^[18,21]

1.1.4 Breast Cancer Metastasis

The primary reason for high mortality rate in patients initially diagnosed with breast cancer is the metastasis. A substantial proportion of these patients (23.3%) develop distant metastasis.^[30] The molecular subtype of breast cancer appears to affect the pattern of metastases. The probability of metastasis in the first five years after the breast cancer diagnosis in TNBC subtype is higher than other histological subtypes. The common sites for breast cancer metastases in order of prevalence are bone, liver, lung, brain and ovary.^[17,30,31] The triple-negative subtype has the tendency to metastasize to distal organs especially lung and brain.^[32]

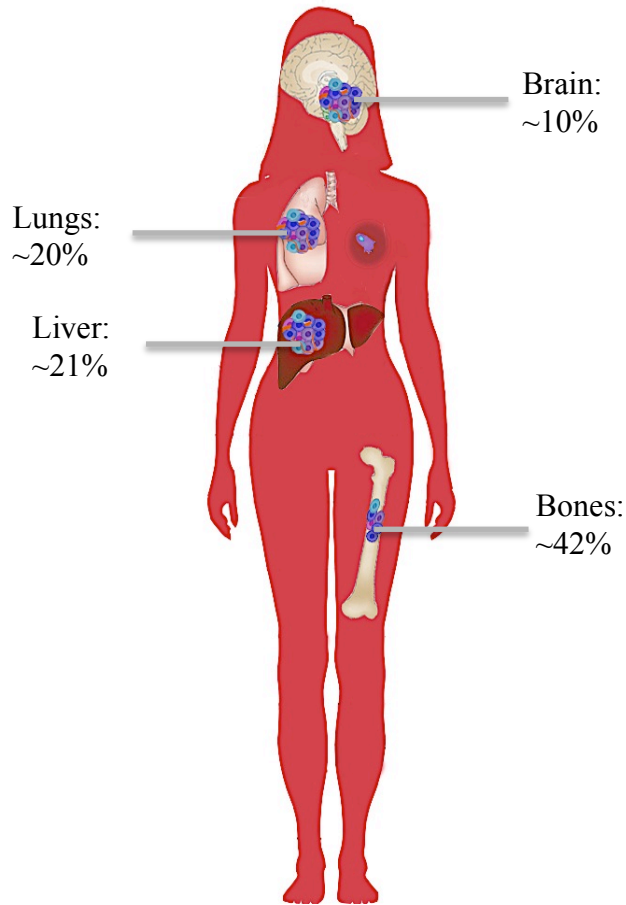


Figure 1-2: Breast cancer patients most commonly die from metastases instead of primary tumor. The common distant sites for breast cancer metastasis are bones, liver, lungs and brain. Main sites of metastasis in breast cancer patients and their incidence are shown.^[31] Adapted from reference 28 and by permission from Macmillan Publishers Ltd: Nature Reviews Cancer, Nguyen *et al.* 9:274-284, copyright© 2009 April Nature Publishing Group

1.1.4.1 Breast Cancer Brain Metastasis

Breast is the second common primary site associated with brain metastasis.^[18] With the advances in controlling primary breast tumor and systemic disease, the treatment of breast cancer brain metastasis (BCBM) has become a crucial component for improving the overall survival and quality of life in these patients.^[33] It is estimated 10-

30% of all breast cancer patients develop brain metastasis, which can either be symptomatic or asymptomatic.^[34,35] An average of 1-year survival can be seen in less than 20% of breast cancer patients from the time of diagnosis with brain metastasis, and approximately 50% of patients die because of the symptoms in their brain.^[34,36,37] Breast cancer subtype has been known to be an independent prognostic factor.

Among different subtypes of breast cancer, HER2 and TNBC have higher risk of brain metastasis. Brain metastases occurs approximately in 10% of breast cancer patients with triple-negative subtype.^[34] Additionally, TNBC has the poorest overall survival rate compared to the other subtypes, as this subtype does not benefit from systemic treatments.^[34,35,38]

The treatment options for patients with BCBM is the same as other histological types of brain metastases.^[34,39] Radiation therapy either as SRS or WBRT modality is an inevitable part of the treatment for BCBM patients. The lack of effective treatment due to the structure of the brain in addition to an increase in the incidence of brain metastasis requires advancing our knowledge about current therapies. So far, improvements in understanding breast cancer subtypes have led to the individualization of systemic treatments, but as these subtypes reach the brain and form metastasis the same radiation dose/fractionation is used. Not only the same radiation protocol is used for all subtypes of breast cancer but all types of brain metastasis regardless of their primary origin. Often, radiosensitivity of primary tumor is not taken into the account for radiation dose prescription; this is despite the fact that brain metastases from breast cancer are relatively more radiosensitive than other primaries i.e. melanoma.^[35,40] The question remains how specific breast cancer subtype would respond to different doses of radiation.

1.1.5 Breast Cancer Brain Metastases Preclinical Models

Preclinical models of breast cancer brain metastases are important for understanding the physiology of cancer and evaluating its response to treatment. For most preclinical brain metastasis models, the cancer cells are directly injected into the

arterial circulation to imitate the metastatic process. This method requires developing cell lines that grow preferentially in the brain when injected into the left ventricle of the beating animal heart.^[41] In this thesis we employed MDA-MB-231-BR, the brain tropic human triple-negative breast cancer cell line. These cells are injected directly into the left ventricle of the heart of female nude mice. The parental cell line (MDA-MB-231P) has been passaged six times in brain metastases and in culture to establish brain seeking cells (MDA-MB-231-BR).^[42] This sub-line shares many characteristics of human brain craniotomy samples such as apoptosis, proliferation and neuro-inflammatory response.^[41]

1.2 Radiation Therapy

Radiation therapy can control rapidly dividing tumor cells (benign or malignant) by creating breaks in their DNA (Deoxyribonucleic Acid). Ionizing radiation (IR) is often considered as a “double-edged sword”, where it can induce mutations in the normal healthy cells while eradicating tumor cell.^[43]

1.2.1 Radiobiology Principles

When IR interacts with cells, it can damage organelles in the cytoplasm, cell membrane and the DNA in the nucleus.^[44] DNA is the central store of our genetic information and an effective target for cell death.^[45] DNA damage induced by IR can result in cellular death or early steps of carcinogenesis depending on dose. Cell death can be an active process through apoptosis (self-programmed death) or passive where cells go through mitosis and manifest irreparable chromosomes.^[26,44] Moreover, cells may maintain their metabolic activity but lose their reproductive capacity (senescence).^[46] On the other hand, cells can repair the induced damage as they have an arsenal of repair proteins. Radiation may induce cell cycle arrest, which gives the cells time to fix the damage.^[44,47] Normal mammalian cells can repair a substantial amount of DNA damage. IR induces wide range of lesions to the DNA such as base damage, single-strand or double-strand breaks.^[46,48] These breaks can be induced either directly through ionization and/or indirectly by transient production of free radicals through water radiolysis process.^[26,45]

1.2.2 DNA Double-Stranded Breaks (DSBs)

DNA double strand-breaks (DSBs) can be induced by an endogenous source, for example products of internal metabolism, or exogenously such as IR. DNA DSBs are the most biologically significant effect of ionizing radiation. It is known that exposure to 1 Gy of IR (photon) produces approximately 30-40 DNA DSBs in diploid mammalian cells.^[45,46,48] DSBs are lesions formed when two opposite strands of the DNA duplex are broken in a distance less than ten base pairs.^[45] The incidence of DSBs is relatively rare compared to other types of DNA damage, but the repair mechanism is more complex. In normal mammalian cells, it takes more than 50 minutes to repair 50% of DSBs after induction, whereas for other DNA damages such as base damage or single-strand break the repair will be achieved in less than 20 minutes.^[47] Following DSBs a cell can take two different pathways to repair the break depending on its status in the cell cycle.^[49]

1.2.2.1 DSBs Detection Techniques

Assessment and quantification of cellular DNA damage is crucial in cancer treatments.^[50] There have been many techniques developed for detecting DNA DSBs, some of which, such as conventional “halo assay” have been replaced by other assays.^[47] Pulsed field electrophoresis (PFGE) and comet assay are two methods that can measure the physical fragmentation of the DNA after the break for both single and double-strand breaks.^[51,52] These techniques use liberated DNA from lysed cells and require radiation dose of >5Gy for a reliable assessment.^[47,51,52] In late 1990's Bonner and Löbrich introduced the γ -H2AX technique to monitor the induction and repair of DSB.^[53,54] Gamma histone 2AX (γ -H2AX) technique is 100 times more sensitive and precise than the other methods and allows investigation of the temporal and spatial induction of DNA DSBs in intact cells and tissue samples. γ -H2AX can be used to detect doses as low as 1.2 mGy.^[45,55] It has been shown that each γ -H2AX focus represents one DSB and consists of hundreds to thousands phosphorylated histone H2AX.^[54,56] A primary antibody against γ -H2AX is used in combination with a secondary fluorescent tag to visualize these foci in a typical immunohistochemistry procedure. Figure 1-3

demonstrates an example of our immunofluorescence staining of γ -H2AX to detect DNA DSB visualized under a confocal microscope. This assay has been employed for a number of applications in diagnosis and assessment of treatment efficacy of cancer.^[57,58] γ -H2AX has also been an attractive *in-vivo* biomarker for detection of malignant cells in blood samples and biopsies.^[58,59] It has been shown that tumors and premalignant lesions demonstrate high amount of endogenous γ -H2AX due to replication stress, dysfunctional telomeres and genomic instability.^[55,60–62] However, one of the caveats of this method is, it does not detect the actual physical break of the DNA, but the cellular activities following the damage. The timing of γ -H2AX foci loss does not precisely agree with the final rejoining of the DNA DSB leading to possible inconsistencies.^[63,64]

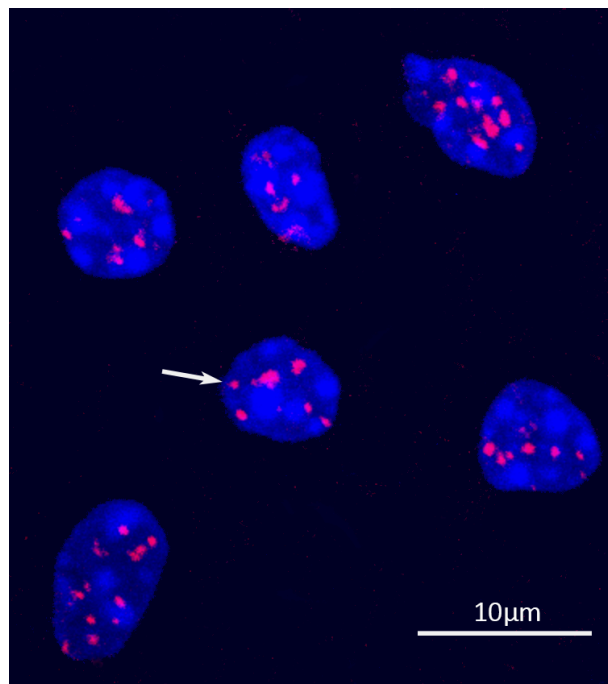


Figure 1-3: Image of mouse brain tissue 30 minutes after receiving \sim 1 Gy, stained with fluorescent anti- γ -H2AX antibody. The arrow is pointing to a focus (red), which represents a DNA DSB. Blue is DAPI counterstain for the nuclei.

1.2.2.2 Role of γ -H2AX

DNA damage happens in the context of chromatin.^[47,58] Chromatin structure consists of DNA and proteins. The fundamental units of chromatin are called nucleosomes. Approximately 145-147 DNA base pairs wrap around four pairs (an octamer) of histone proteins (H2A, H2B, H3 and H4) to form a nucleosome.^[65] Following DNA DSBs from IR, the cell senses the damage via ATM (Ataxia telangiectasia mutated), a member of the phosphoinositide 3-kinase-related-kinase (PIKK) family.^[66] As a result, the histone variant H2A, H2AX (~10% of H2A), are rapidly phosphorylated in the vicinity of the DSB and the chromatin around the break.^[63] The phosphorylated H2AX is termed γ -H2AX. Figure 1-4 demonstrates the cascade of activation of H2AX. Phosphorylation of H2AX is also controlled by other PIKK members such as ATR (ATM- and Rad3-related) and DNA-PKcs (DNA-dependent protein kinase catalytic subunit).^[66] However, it is mostly ATM that governs the phosphorylation of H2AX following DNA DSB.^[63] γ -H2AX serves as a beacon for the cell and triggers DNA damage response (DDR), recruiting detection, signaling and repair proteins to the DSB site.^[49] For each DSB, hundreds to thousands of nearby H2AX molecules get phosphorylated to form a focus.^[54,63] The number of foci is known to correlate linearly with IR dose in most cell types.^[61,67] However, at high radiation doses such as 2 Gy, detecting individual focus shortly after IR (~30 minutes) is not possible due to overlapping foci and diffuse covering of γ -H2AX in tumor nuclei.^[54,68,69] Counting discrete foci either manually or automatically on 3D images acquired from confocal microscopy is the common technique employed for low doses of radiation.^[61,70] At higher radiation doses where finding separate foci is challenging, intensity quantification techniques such as flow cytometry in cells or image intensity from fluorescence-stained tissue samples are commonly used.^[68-71] It should be noted that γ -H2AX is a time sensitive marker. The phosphorylation of H2AX starts within 3 minutes after IR and gets to the maximum level approximately 30 minutes after IR exposure.^[53-55] As DNA DSBs are repaired, γ -H2AX either gets dephosphorylated or removed from the chromatin.^[56,61,63] Resolving γ -H2AX over time allows us to assess DNA repair kinetics and mechanism of action.

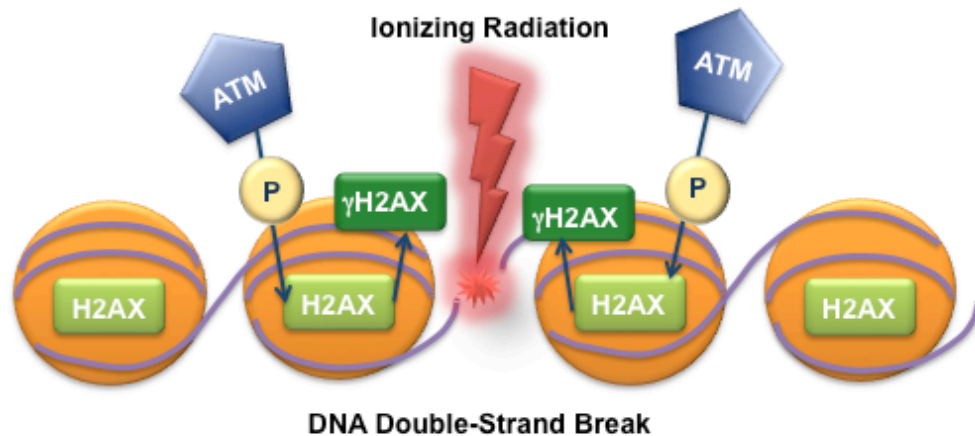


Figure 1-4: DNA is wrapped around core histone proteins. Upon DNA double-strand break, one of the histone proteins, H2AX, gets rapidly phosphorylated by ATM adjacent to the site of damage. The phosphorylated H2AX is termed γ -H2AX.

1.2.3 Radiation Therapy Dose-Response Relationship

One of the concerns in clinical radiobiology is the response of tumor and normal tissue to radiation doses. A sigmoid radiation dose-response curve has been considered for both tumor control and normal tissue complications.^[26,46,72] In this relation, the response to radiation tends toward zero as dose approaches zero and tends toward 100% for large radiation doses.^[26,45] The response of tumors to radiation can be measured by different end-points such as local tumor control and tumor regrowth delay.

While same radiation dose/fractionation is prescribed for the treatment of all brain metastasis, patients outcomes are different depending on the origin of the tumor.^[40,73,74] A major factor is that tumors from different origins have different radiosensitivity and steepness of the dose-response curve. Inter and intra-patient tumor heterogeneity are also found within one type of cancer.^[75] These differences can be partly explained by dissimilarities in growth kinetics, loss of apoptotic or checkpoint genes, DNA damage

and repair pattern and the microenvironment influenced by hypoxia and angiogenesis.^[45] All of these factors play a crucial role in determining the response of the tumors to RT.

In-vivo dose-response studies in preclinical models have the advantage of both inherent tumor radiosensitivity and also the influence of the tumor's microenvironment. To be able to design experiments using human cancer cell lines in an animal model that can recapitulate clinical dose-response challenges, simulating clinical scenarios in the lab plays a key role.^[76] To deliver clinically relevant radiation doses, biological effective dose (BED) formula helps to convert the clinical dose/fractionation regimen to practical dose/fractionation on the models while having the same biological effect.^[77,78] BED is a measure of the biological dose delivered by the specific total dose and fractionation:

$$BED = nd \left[1 + \frac{d}{\frac{\alpha}{\beta}} \right], \quad (1-1)$$

Where n is the number of fractions, d is the dose per fraction and $\frac{\alpha}{\beta}$ is a radiosensitivity parameter of the tissue.^[45,79]

1.2.4 Preclinical Radiation Therapy Devices

To be able to investigate and validate some of the clinical and technological evolutions in the field of cancer and radiation therapy, radiation delivery units are needed for preclinical models. These devices enable us to mimic human radiotherapy conditions. For many decades, small animal models received radiation using Cs¹³⁷ or Co⁶⁰ irradiator boxes or clinical linear accelerators. Improvements in technology and the need for precise and accurate dose delivery motivated investigators to design and build imaging and radiation therapy devices dedicated to preclinical studies. Nowadays, preclinical machines capable of on-board imaging along with a range of beam energies (kV) appropriate for the size of small animals are available.^[80]

Many groups have developed sophisticated research systems for precise small animal radiation. These machines such as SARRP (John Hopkins), X-rad 225Cx

(Princess Margaret Hospital) and modified micro-CT/RT scanner (Stanford University and University of Western Ontario) are the most commonly used devices in this field.^[80,81]

Modified Micro-CT/RT scanner has the advantage of high-quality on-board imaging, computerized asymmetric collimator and live animal monitoring.^[81] On-board imaging refers to the imaging unit that is installed on the treatment machine and allows imaging before treatment to confirm a match between treatment and planned setup. The combination of image guidance and asymmetric collimators allow irradiating small sub-regional fields in three-dimensions. This unit has been used to study the effect of radiation therapy on normal tissues and will be employed in this thesis for our tumor model.^[82]

Precision and accuracy are significant factors in small animal radiation therapy. For instance, the width of the mouse brain is approximately 1 cm in its largest dimension, and sub-millimeter precision is required to irradiate sub-regions of the brain. Considering the scale of animal models, error margins should be less than 0.2 mm to deliver a precise conformal dose.^[83] Accurate set-up and immobilization, help with precise radiation dose delivery.^[84] In the clinical setting, external stabilization devices such as head holder, bite blocks and thermoplastics are often used specifically for head and neck cases to minimize the patient's movement and maximize the reproducibility of the treatment set-up.^[85] In preclinical setting, restrainer devices are needed to position the animal in the desirable setting while maintaining animal's body temperature and monitoring it during radiation dose delivery.

1.3 Magnetic Resonance Imaging (MRI)

Magnetic resonance imaging (MRI) is currently the standard imaging modality for detecting brain metastasis, radiation treatment planning and follow-up in patients. It has greater sensitivity in comparison with contrast enhanced CT for detecting small brain lesions.^[22] MRI is a noninvasive imaging technique, which requires no IR and results in

high soft-tissue contrast. Gadolinium-DTPA (Gd) is the common contrast agent for detecting brain lesions.^[86] In patients with brain metastases, this agent can penetrate leaky and disrupted tumor-brain barriers, resulting in tumors with hyper-intensities.^[87]

In brain metastases preclinical models, 3D MRI allows monitoring tumors temporally and spatially.^[88,89] More specifically, this imaging modality is useful in assessing tumor volume and morphology before and after radiation to investigate the effect of treatment.^[90] Sequential MR images followed by histological analysis are used in this thesis to investigate response of the tumors to the radiation at the small animal and cellular level.

1.3.1 Balanced Steady State Free Precession (bSSFP) MRI Sequence

The balanced steady state free precession (bSSFP) MRI sequence was primarily used for cardiac imaging but recently has been employed to image other sites.^[91,92] The most important feature of this sequence is its ability to produce high-resolution images while keeping high signal-to-noise ratio in a reasonable scan time. The contrast in bSSFP is dependent on the ratio of tissue T2 relaxation rate to its T1 relaxation rate. This ratio means that in this sequence images of fat and fluid, which have different T1 and T2 relaxation time but have the same ratio of T2/T1, appear as bright regions.^[91,92]

The utility of the bSSFP sequence in the imaging of preclinical models and brain metastasis has been explored over the past few years.^[93-95] A large fraction of brain metastases are not permeable to Gd at early time-points and would not optimally be imaged with T1 or T2 post-contrast sequences. Percy *et al.* have shown that pre-contrast bSSFP can detect brain metastasis regardless of their permeability status and is a sensitive sequence to be used for brain metastases in preclinical models.^[88,96] In this thesis, bSSFP MRI sequence will be used to evaluate the response of brain metastases to radiation longitudinally.

1.4 Three-Dimensional (3D) Printing Technology

Three-dimensional (3D) printing is rapidly being developed and adopted. This technology allows building tangible 3D solid objects from virtual designs. There are three main steps to fabricate the desirable object: 1) Modeling 2) Printing 3) Processing. Manual 3D modeling is usually done using computer aided design (CAD) (e.g. AutoCad® and SolidWorks™). The drawing will be exported as Stereolithography (.STL) file format to be readable by the printer. The printer software interprets the .STL model to thin cross-sectional layers. The 3D-printer used in this thesis is Object30 Pro, an acrylic based plastic printer. It lays down thin horizontal layers (28 microns) of liquid resin, which would be cured by ultraviolet light. The layers will be fused together automatically and create the final object. The processing step consists of smoothing the surface of the object with sand paper and using a water jet to remove the residual material. Figure 1-5 shows the processes involved in 3D-printing. We will be using 3D-printing technology in our small animal brain irradiation studies.

Three-dimensional printing technology brings benefits over the conventional manufacturing method. It can be used to create customized objects with varying complexities from virtual designs in an inexpensive and timely manner. This technology has been used in various sectors such as industry, medicine, forensic science and education and will have a great influence on many fields in the near future.^[97] Interestingly, this technology has found its way to preclinical laboratories to construct objects needed for experimental designs.^[98,99] Furthermore, the nature of the digital file offers new prospects for sharing and collaborating with researchers. This allows printing the same devices and/or modifying the existing design to suit the experimental setting.

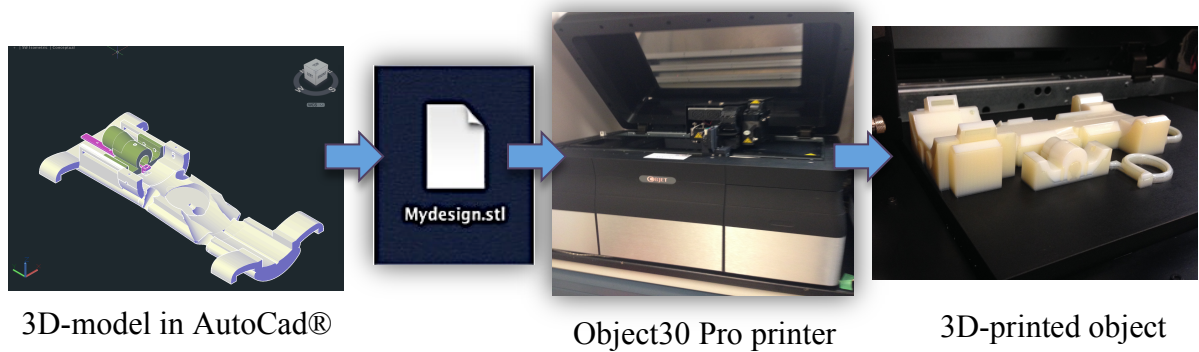


Figure 1-5: Processes involved in 3D-printing. Modeling is done in AutoCAD and exported as .STL format. The 3D-printer converts the digital file to thin cross-sectional layers. The final 3D-printed object is shown on the 3D-printer tray. A final processing step is needed to remove residual material from the object.

1.5 Thesis Objectives and Outline

The main goal of this thesis is to quantify the response of breast cancer brain metastasis to different radiation doses. To achieve this, we had two specific objectives:

1. To improve and histologically evaluate radiation targeting accuracy for mouse hemi-brain radiation therapy on the micro-CT/RT unit.
2. To quantify the acute amount of induced DSBs in a breast cancer brain metastasis model for different radiation doses and evaluate dose-response in the brain metastasis model longitudinally after treatment.

Objective 1 is addressed in Chapter 2 where we utilized 3D-printing technology for animal immobilization, enabling studies in objective 2. We designed a mouse restrainer for the purpose of half-brain radiation and used 3D-printer for the fabrication.

The device was evaluated for targeting accuracy using immunohistochemistry. This work has been submitted to the journal of *Medical Physics*.

Chapter 3 discusses the response of breast cancer brain metastases to different radiation doses utilizing our 3D-printed device. The amount of induced (acute) and residual (longitudinal) DNA double-strand breaks was quantified for both tumor and mouse normal brain cells. bSSFP MR imaging was used to determine the *in-vivo* response of tumors in the mouse model following hemi-brain radiation. A manuscript based on this chapter is in preparation.

In chapter 4, major findings of this thesis are summarized. This chapter discusses the limitations of the present study and future investigations are proposed.

1.6 References

1. American Cancer Society. Cancer Facts & Figures 2015. 2015;
2. Canada S. Canadian Cancer Statistics Special topic : Predictions of the future burden of cancer in Canada. 2015;
3. Siegel RL, Miller KD, Jemal A. Cancer Statistics, 2015. *CA Cancer J Clin* 2015;65(1):5–29.
4. Bertos N, Park M. Breast cancer—one term, many entities? *J Clin Invest* 2011;121(10):3789–96.
5. Li CI, Uribe DJ, Daling JR. Clinical characteristics of different histologic types of breast cancer. *Br J Cancer* 2005;93(9):1046–52.
6. Yersal O, Barutca S. Biological subtypes of breast cancer: Prognostic and therapeutic implications. *World J Clin Oncol* 2014;5(3):412–24.
7. Schnitt SJ. Classification and prognosis of invasive breast cancer: from morphology to molecular taxonomy. *Mod Pathol* 2010;23 Suppl 2(S2):S60–4.
8. Harbeck N, Thomssen C, Gnant M. St. Gallen 2013: Brief preliminary summary of the consensus discussion. *Breast Care* 2013;8(2):102–9.
9. Inic Z, Zegarac M, Inic M, Markovic I, Kozomara Z, Djuricic I, et al. Difference between Luminal A and Luminal B Subtypes According to Ki-67, Tumor Size, and Progesterone Receptor Negativity Providing Prognostic Information. *Clin Med Insights Oncol* 2014;8:107–11.
10. Arteaga CL, Sliwkowski MX, Osborne CK, Perez E a., Puglisi F, Gianni L. Treatment of HER2-positive breast cancer: current status and future perspectives. *Nat Rev Clin Oncol* 2011;9(1):16–32.
11. Ovcaricek T, Frkovic SG, Matos E, Mozina B, Borstnar S. Triple negative breast cancer - prognostic factors and survival. *Radiol Oncol* 2010;45(1):46–52.

12. Kim K, Lee E, Lee J, Bae J, Korea Breast Cancer Society . Clinicopathologic Signature of TNBC Patients with Good Prognosis. *Cancer Res* 2009;69(24):4065–4065.
13. Anders C, Carey L. Understanding and treating triple-negative breast cancer. *Oncol (willist Park NY)* 2008;22(11):1233–43.
14. MacDonald IC, Groom AC, Chambers AF. Cancer spread and micrometastasis development: Quantitative approaches for in vivo models. *BioEssays* 2002;24(10):885–93.
15. Wong SY, Hynes RO. Lymphatic or hematogenous dissemination: How does a metastatic tumor cell decide? *Cell Cycle* 2006;5(8):812–7.
16. Joyce J a, Pollard JW. Microenvironmental regulation of metastasis. *Nat Rev Cancer* 2009;9(4):239–52.
17. Chambers AF, Groom AC, MacDonald IC. Dissemination and growth of cancer cells in metastatic sites. *Nat Rev Cancer* 2002;2(8):563–72.
18. Gavrilovic IT, Posner JB. Brain metastases: Epidemiology and pathophysiology. *J Neurooncol* 2005;75(1):5–14.
19. Smith S, Theodorescu D. Learning therapeutic lessons from metastasis supressor proteins. *Nat Rev Cancer* 2009;9:253–64.
20. Owonikoko TK, Arbiser J, Zelnak A, Shu H-KG, Shim H, Robin AM, et al. Current approaches to the treatment of metastatic brain tumours. *Nat Rev Clin Oncol* 2014;11(4):203–22.
21. Patchell R a. The management of brain metastases. *Cancer Treat Rev* 2003;29(6):533–40.
22. Lu-Emerson C, Eichler A. Brain Metastases. *Neuro Oncol* 2012;18(2):295–311.

23. Lee JJ, Lotze MT. Molecular basis of metastasis. *N Engl J Med* 2009;360(16):1679; author reply 1679–80.
24. Zhang X, Zhang W, Cao W-D, Cheng G, Liu B, Cheng J. A Review of Current Management of Brain Metastases. *Ann Surg Oncol* 2012;19(3):1043–50.
25. Khuntia D. Review Article Contemporary Review of the Management of Brain Metastasis with Radiation. *Adv Neurosci* 2015;2015:13.
26. Steel GG. *Basica Clinical Radiobiology*. 4th ed. London: Hodder Education; 2009.
27. McTyre E, Scott J, Chinnaiyan P. Whole brain radiotherapy for brain metastasis. *Surg. Neurol. Int.* 2013;4(Suppl 4):S236–44.
28. Kondziolka D, Niranjan A, Flickinger JC, Lunsford LD. Radiosurgery with or without whole-brain radiotherapy for brain metastases: the patients' perspective regarding complications. *Am J Clin Oncol* 2005;28(2):173–9.
29. Ranjan T, Abrey LE. Current management of metastatic brain disease. *Neurotherapeutics* 2009;6(3):598–603.
30. Maxmen A. The hard facts. *Nature* 2012;485(7400):S50–1.
31. Vona-Davis L, Rose DP, Gadiyaram V, Ducatman B, Hobbs G, Hazard H, et al. Breast cancer pathology, receptor status, and patterns of metastasis in a rural appalachian population. *J Cancer Epidemiol* 2014;2014.
32. Andreopoulou E, Schweber SJ, Sparano JA. Therapies for triple negative breast cancer. *Expert Opin Pharmacother* 2015;16(7):983–98.
33. Kodack DP, Askoxylakis V, Ferraro GB, Fukumura D, Jain RK. Emerging Strategies for Treating Brain Metastases from Breast Cancer. *Cancer Cell* 2015;27(2):163–75.
34. Gil-Gil MJ, Martinez-Garcia M, Sierra a., Conesa G, Del Barco S, González-Jimenez S, et al. Breast cancer brain metastases: A review of the literature and a

- current multidisciplinary management guideline. *Clin Transl Oncol* 2014;16(5):436–46.
35. De Ieso PB, Schick U, Rosenfelder N, Mohammed K, Ross GM. Breast cancer brain metastases – A 12 year review of treatment outcomes. *The Breast* 2015;3–10.
 36. Cheng X, Hung M-C. Breast cancer brain metastases. *Cancer Metastasis Rev* 2007;26(3-4):635–43.
 37. Niikura N, Hayashi N, Masuda N, Takashima S, Nakamura R, Watanabe KI, et al. Treatment outcomes and prognostic factors for patients with brain metastases from breast cancer of each subtype: A multicenter retrospective analysis. *Breast Cancer Res Treat* 2014;147(1):103–12.
 38. Lin NU, Claus E, Sohl J, Razzak AR, Arnaout A, Winer EP. Sites of Distant Relapse and Clinical Outcomes in Patients with Metastatic Triple-Negative Breast Cancer: High Incidence of Central Nervous System Metastases. 2010;113(10):2638–45.
 39. Wiggendaad R, Kanter AV De, Kal HB, Taphoorn M, Vissers T, Struikmans H. Dose-effect relation in stereotactic radiotherapy for brain metastases. A systematic review. *Radiother Oncol* 2011;98(3):292–7.
 40. Nieder C, Walter K. Dose / effect relationships for brain metastases. *Survival (Lond)* 1998;346–50.
 41. Lin NU, Amiri-Kordestani L, Palmieri D, Liewehr DJ, Steeg PS. CNS metastases in breast cancer: Old challenge, new frontiers. *Clin Cancer Res* 2013;19(23):6404–18.
 42. Yoneda T, Williams PJ, Hiraga T, Niewolna M, Nishimura R. A bone-seeking clone exhibits different biological properties from the MDA-MB-231 parental human breast cancer cells and a brain-seeking clone in vivo and in vitro. *J Bone Miner Res* 2001;16(8):1486–95.

43. Brenner DJ. 2011 FAILLA AWARD LECTURE: Exploring Two Two-Edged Swords David. *Radiat Res* 2012;178(1):7–16.
44. Cohen-Jonathan E, Bernhard EJ, McKenna WG. How does radiation kill cells? *Curr Opin Chem Biol* 1999;3(1):77–83.
45. Hall EJ, Giaccia AJ. *Radiobiology for the Radiologist*. 7th ed. Philadelphia: Wolters Kluwer Health/Lippincott Williams & Wilkins; 2012.
46. RADIATION BIOLOGY: A HANDBOOK FOR TEACHERS AND STUDENTS. Vienna: INTERNATIONAL ATOMIC ENERGY AGENCY; 2010.
47. Lavelle C, Foray N. Chromatin structure and radiation-induced DNA damage: from structural biology to radiobiology. *Int J Biochem Cell Biol* 2014;49(how):84–97.
48. Thrall DE. Biologic basis of radiation therapy. *Vet Clin North Am Small Anim Pract* 1997;27(1):21–35.
49. Thompson LH. Recognition, signaling, and repair of DNA double-strand breaks produced by ionizing radiation in mammalian cells: The molecular choreography. *Mutat Res - Rev Mutat Res* 2012;751(2):158–246.
50. Motalleb G, Sanadgol N, Estakhr J, Shahraki E. Methods for DNA strand breaks detection. *Res J Appl Sci Eng Technol* 2012;4(13):1888–94.
51. Olive PL, Banáth JP. The comet assay: a method to measure DNA damage in individual cells. *Nat Protoc* 2006;1(1):23–9.
52. Kumari S, Rastogi RP, Singh KL, Singh SP. Dna Damage : Detection Strategies. *EXCLI J* 2008;7:44–62.
53. Rogakou EP, Pilch DR, Orr AH, Ivanova VS, Bonner WM. DNA Double-stranded Breaks Induce Histone H2AX Phosphorylation on Serine 139. *J Biol Chem* 1998;273(10):5858–68.

54. Pilch DR, Sedelnikova O a, Redon C, Celeste A, Nussenzweig A, Bonner WM. Characteristics of gamma-H2AX foci at DNA double-strand breaks sites. *Biochem Cell Biol* 2003;81:123–9.
55. Ivashkevich A, Redon CE, Nakamura AJ, Martin RF, Martin OA. Use of the γ -H2AX assay to monitor DNA damage and repair in translational cancer research. *Cancer Lett* 2013;487:109–13.
56. Kuo LJ, Yang LX. Gamma-H2AX - a novel biomarker for DNA double-strand breaks. *In Vivo (Brooklyn)* 2008;22(3):305–9.
57. Redon CE, Nakamura AJ, Martin OA, Parekh PR, Weyemi US, Bonner WM. Recent developments in the use of γ -H2AX as a quantitative DNA double-strand break biomarker. *3(2)*:168–74.
58. Bonner WM. γ -H2AX and other histone post-translational modifications in the clinic. *2013;1819(7)*:743–56.
59. Pouliliou S, Koukourakis MI. Gamma histone 2AX (γ -H2AX) as a predictive tool in radiation oncology. *Biomarkers* 2014;19:167–80.
60. Sedelnikova O a, Bonner WM. γ H2AX in Cancer Cells ND ES SC RIB. *2006;(December)*:2909–13.
61. Bonner WM, Redon CE, Dickey JS, Nakamura AJ, Olga A, Solier S, et al. γ H2AX and cancer. *Cancer* 2011;8(12):957–67.
62. Cornelissen B, Kersemans V, Darbar S, Thompson J, Shah K. Europe PMC Funders Group Imaging DNA damage in vivo using γ H2AX-targeted immunoconjugates. *2012;71(13)*:4539–49.
63. Kinner A, Wu W, Staudt C, Iliakis G. Gamma-H2AX in recognition and signaling of DNA double-strand breaks in the context of chromatin. *Nucleic Acids Res* 2008;36(17):5678–94.

64. Löbrich M, Shibata A, Beucher A, Fisher A, Ensminger M, Goodarzi A a., et al. γ H2AX foci analysis for monitoring DNA double-strand break repair: Strengths, limitations and optimization. *Cell Cycle* 2014;9(4):662–9.
65. Talbert PB, Henikoff S. Histone variants--ancient wrap artists of the epigenome. *Nat Rev Mol Cell Biol* 2010;11(4):264–75.
66. Rothkamm K, Horn S. γ -H2AX as protein biomarker for radiation exposure. *Ann Ist Super Sanita* 2009;45(3):265–71.
67. Barnard S, Bouffler S, Rothkamm K. The shape of the radiation dose response for DNA double-strand break induction and repair. *Genome Integr* 2013;4(1):1.
68. Hernández L, Terradas M, Martín M, Tusell L, Genescà A. Highly sensitive automated method for DNA damage assessment: Gamma-H2AX foci counting and cell cycle sorting. *Int J Mol Sci* 2013;14:15810–26.
69. Yu TY, Chu EHM, Lambur H, Olive PL. Expression of phosphorylated histone H2AX in cultured cell lines following exposure to X-rays. *Int J Radiat Biol* 2003;79(5):351–68.
70. Anderson D, Andrais B, Mirzayans R, Siegbahn E a, Fallone BG, Warkentin B. Comparison of two methods for measuring γ -H2AX nuclear fluorescence as a marker of DNA damage in cultured human cells: applications for microbeam radiation therapy. *J Instrum* 2013;8:6008–16.
71. Ismail IH, Wadhra TI, Hammarsten O. An optimized method for detecting gamma-H2AX in blood cells reveals a significant interindividual variation in the gamma-H2AX response among humans. *Nucleic Acids Res* 2007;35(5).
72. Bolus NE. Basic Review of Radiation Biology and Terminology. *Nucl Med Technol* 2001;29(2):67–74.
73. Bender ET, Tomé W a. Distribution of brain metastases: Implications for non-uniform dose prescriptions. *Br J Radiol* 2011;84(1003):649–58.

74. Nieder C, Berberich W, Schnabel K. Tumor-related prognostic factors for remission of brain metastases after radiotherapy. *Int. J. Radiat. Oncol. Biol. Phys.* 1997;39(1):25–30.
75. Moding EJ, Kastan MB, Kirsch DG. Radiation, Strategies for optimizing the response of cancer and normal tissues to. *Nat Rev Drug Discov* 2012;29(6):997–1003.
76. Butterworth KT, Prise KM, Verhaegen F. Small animal image-guided radiotherapy: status, considerations and potential for translational impact. *Br J Radiol* 2015;88(1045):20140634.
77. Fowler JF. 21 Years of biologically effective dose. *Br J Radiol* 2010;83(991):554–68.
78. Marples B. *The Management of Gynecologic Cancers:Radiobiology*. 2013.
79. Woditschka S, Evans L, Duchnowska R, Reed LT, Palmieri D, Qian Y, et al. DNA double-strand break repair genes and oxidative damage in brain metastasis of breast cancer. *J Natl Cancer Inst* 2014;106:1–13.
80. Verhaegen F, Granton P, Tryggestad E. Small animal radiotherapy research platforms. *Phys Med Biol* 2011;56(12):R55–83.
81. Jensen MD, Hrinivich WT, Jung J a, Holdsworth DW, Drangova M, Chen J, et al. Implementation and commissioning of an integrated micro-CT/RT system with computerized independent jaw collimation. *Med Phys* 2013;40(8):0817061–08170613.
82. Thind K, Jensen MD, Hegarty E, Chen AP, Lim H, Martinez-Santesteban F, et al. Mapping metabolic changes associated with early Radiation Induced Lung Injury post conformal radiotherapy using hyperpolarized ¹³C-pyruvate Magnetic Resonance Spectroscopic Imaging. *Radiother Oncol* 2014;110(2):317–22.

83. Kiehl EL, Stojadinovic S, Malinowski KT, Limbrick D, Jost SC, Garbow JR, et al. Feasibility of small animal cranial irradiation with the microRT system. *Med Phys* 2008;35(10):4735–43.
84. Armour M, Ford E, Iordachita I, Wong J. CT Guidance is Needed to Achieve Reproducible Positioning of the Mouse Head for Repeat Precision Cranial Irradiation. *Radiation Res* 2010;173(1):119–23.
85. Perez CA, Brady LW. Perez and Brady's principles and practice of radiation oncology. 6th ed. Philadelphia: Wolters Kluwer Health/Lippincott Williams & Wilkins; 2013.
86. Anzalone N, Gerevini S, Scotti R, Vezzulli P, Picozzi P. Detection of cerebral metastases on magnetic resonance imaging: intraindividual comparison of gadobutrol with gadopentetate dimeglumine. *Acta radiol* 2009;50(8):933–40.
87. Bellin MF, Van Der Molen AJ. Extracellular gadolinium-based contrast media: An overview. *Eur J Radiol* 2008;66(2):160–7.
88. Perera M, Ribot EJ, Percy DB, Mcfadden C, Simeanea C, Palmieri D, et al. In Vivo Magnetic Resonance Imaging for Investigating the Development and Distribution of Experimental Brain Metastases due to Breast Cancer. *Transl Oncol* 2012;5(3):217–25.
89. Zhou H, Chen M, Zhao D. Longitudinal MRI Evaluation of Intracranial Development and Vascular Characteristics of Breast Cancer Brain Metastases in a Mouse Model. *PLoS One* 2013;8(4).
90. Gazdzinski LM, Cormier K, Lu FG, Lerch JP, Wong CS, Nieman BJ. Radiation-induced alterations in mouse brain development characterized by magnetic resonance imaging. *Int J Radiat Oncol Biol Phys* 2012;84(5):e631–8.
91. Scheffler K, Lehnhardt S. Principles and applications of balanced SSFP techniques. *Eur Radiol* 2003;13(11):2409–18.

92. Bhosale P, Ma J, Choi H. Utility of the FIESTA pulse sequence in body oncologic imaging: review. *AJR Am J Roentgenol* 2009;192(6 Suppl):83–93.
93. Bernas LM, Foster PJ, Rutt BK. Imaging iron-loaded mouse glioma tumors with bSSFP at 3 T. *Magn Reson Med* 2010;64(1):23–31.
94. Mallett CL, Mcfadden C, Chen Y, Foster PJ. Migration of iron-labeled KHYG-1 natural killer cells to subcutaneous tumors in nude mice, as detected by magnetic resonance imaging. *Cytotherapy* 2012;14(6):1–9.
95. Perera M, Ribot EJ, Percy DB, McFadden C, Simeanea C, Palmieri D, et al. In Vivo Magnetic Resonance Imaging for Investigating the Development and Distribution of Experimental Brain Metastases due to Breast Cancer. *Transl Oncol* 2012;5(3):217–25.
96. Percy DB, Ribot EJ, Chen Y, McFadden C, Simeanea C, Steeg PS, et al. In Vivo Characterization of Changing Blood-Tumor Barrier Permeability in a Mouse Model of Breast Cancer Metastasis. *Invest Radiol* 2011;46(11):718–25.
97. Chen C, Erkal JL, Gross BC, Lockwood SY, Spence DM. Evaluation of 3D Printing and Its Potential Impact on Biotechnology and the Chemical Sciences. *Anal Chem* 2014;86(7):3240–53.
98. Zhang L, Yuan H, Burk LM, Inscoe CR, Hadsell MJ, Chtcheprov P, et al. Image-guided microbeam irradiation to brain tumour bearing mice using a carbon nanotube x-ray source array. *Phys Med Biol* 2014;59(5):1283–303.
99. Bache ST, Juang T, Belley MD, Koontz BF, Adamovics J, Yoshizumi TT, et al. Investigating the accuracy of microstereotactic-body-radiotherapy utilizing anatomically accurate 3D printed rodent-morphic dosimeters. *Med Phys* 2015;42(2):846–55.

Chapter 2

2 Immunohistochemical Evaluation of Mouse Brain Irradiation Targeting Accuracy with 3D-Printed Immobilization Device

This chapter is adapted from the technical note, “Immunohistochemical evaluation of mouse brain irradiation targeting accuracy with 3D-printed immobilization device” under review in *Journal of Medical Physics*, by Zarghami N, Jensen MD, Talluri S, Foster PJ, Chambers AF, Dick FA and Wong E.

2.1 Introduction

More than 50 percent of cancer patients receive IR as a main part of their treatment.^[1] Over the last few decades, sophisticated and computerized treatment planning, dose delivery and on-board imaging systems have been introduced and are used routinely. The biological responses of tumor and normal tissue to radiation therapy can be investigated using animal models. Accurate simulation of the patient’s treatment scenario on small animals in laboratories will facilitate translating experimental results to the clinical setting and help further our understanding of radiobiology.

Many groups have developed sophisticated preclinical radiation devices, which are capable of treating sub-regional fields using technologies such as on-board cone beam CT (CBCT). Some devices have integrated bioluminescence tomography while others computerized collimators.^[2-5] Indeed, these cutting-edge devices have enabled researchers to investigate some of the current radiobiological challenges and deliver more complex dose distribution. However, another challenge for accurate radiation dose delivery on live animals is their set-up and positioning. While accuracies for radiotherapy in the clinical settings have been elucidated^[6], analogous specifications for small animals are not yet available. Radiation treatment is commonly performed on sedated animals, but unconstrained anatomical structures complicate positioning and restraining devices are needed for accurate targeting.

Several groups have developed stereotactic holders to improve dose delivery.^[7-9] Moreover, sophisticated commercial devices are available for different small-animal imaging machines.^[10] While all these stereotactic holders have the same purpose of improving animal positioning, they may lack some features for some small animal radiotherapy treatment situations. Such features may include physiological monitoring, animal warming, and the capability for fine position adjustments. Commercially available devices have tended to be designed for imaging rather than radiotherapy. More importantly, traditional fabrication methods may not be economical, especially if several customized variations of a stereotactic holder are required. To allow investigators to optimally position the animal for each treatment site and minimize trauma, it is desirable to economically fabricate multiple external holders for small animal radiation therapy.

In this technical note, we introduce a completely 3-dimensional (3D) printed mouse head holder for a micro-CT/RT system. We investigate the feasibility of using 3D printing technology to make a head holder and then evaluate the head holder's capability for precise mouse brain irradiation. The targeting accuracy is verified with half brain irradiation, using fluorescent immunohistochemical staining for phosphorylated histone H2AX, γ -H2AX, a marker for DNA double-strand breaks^{[11][12]}, on frozen mouse brain sections. γ -H2AX is a sensitive bio-dosimeter and can detect radiation doses as low as 1.2mGy.^[13] This novel device demonstrates the potential application of 3D-printing to small animal experimental platforms.

2.2 Methods and Materials

2.2.1 Head Holder Design and 3D-Printing

The stereotactic mouse head holder was designed for the GE eXplore CT 120 (GE Healthcare, Milwaukee, WI, USA) preclinical imaging system rat couch. This unit has been modified to be capable of small animal imaging and irradiation with on-line image guidance and multiple collimated irradiation fields.^[2]

To size the stereotactic holder, mouse gross anatomical measurements were done on 6-8 week old C57BL/6 and NU-Foxn1^{nu} (Charles River Laboratories, Wilmington, MA) mice. The mouse head holder was designed using AutoCADTM 2014 (Autodesk, Inc. San Rafael, CA, USA) (Figure 2-1a). The head holder design has integrated anesthesia gas delivery and respiration pillow sensor. The nose cone position can be adjusted according to the size of the mouse snout and connects to a commercially available Mapleson-D (Patterson Scientific, USA) for anesthetic gas. The respiration pillow sensor is placed under the abdomen of the animal and its rate can be monitored during the procedure. The mouse incisors are placed in a bite bar inside of the nose cone. The bite bar and two length-adjustable ear bars immobilize and orient the head in the desired position. The 5° inclined bed allows the mouse to be in a neutral position while keeping the head level with the axis of gantry rotation. There are indents for all four paws and the tail of the animal to ensure reproducible set-up. A separate hot water circulation is wrapped around animal's body to maintain its body temperature.

The drawing was exported as three separate parts: bed body, nose cone and bite bar. The stereolithography (.STL) format was imported to ObjectStudio Software (Stratasys, Inc. Rehovot, Israel) to convert the drawing to 3D layer modeling. The fabrication was done with Objet30Pro printer (Stratasys Inc. Rehovot, Israel), using an ultraviolet cured, acrylic based plastic (Verowhite Plus). The head holder was post-processed with a water jet to remove excessive supporting materials and the holes were threaded for screws (Figure 2-1b).

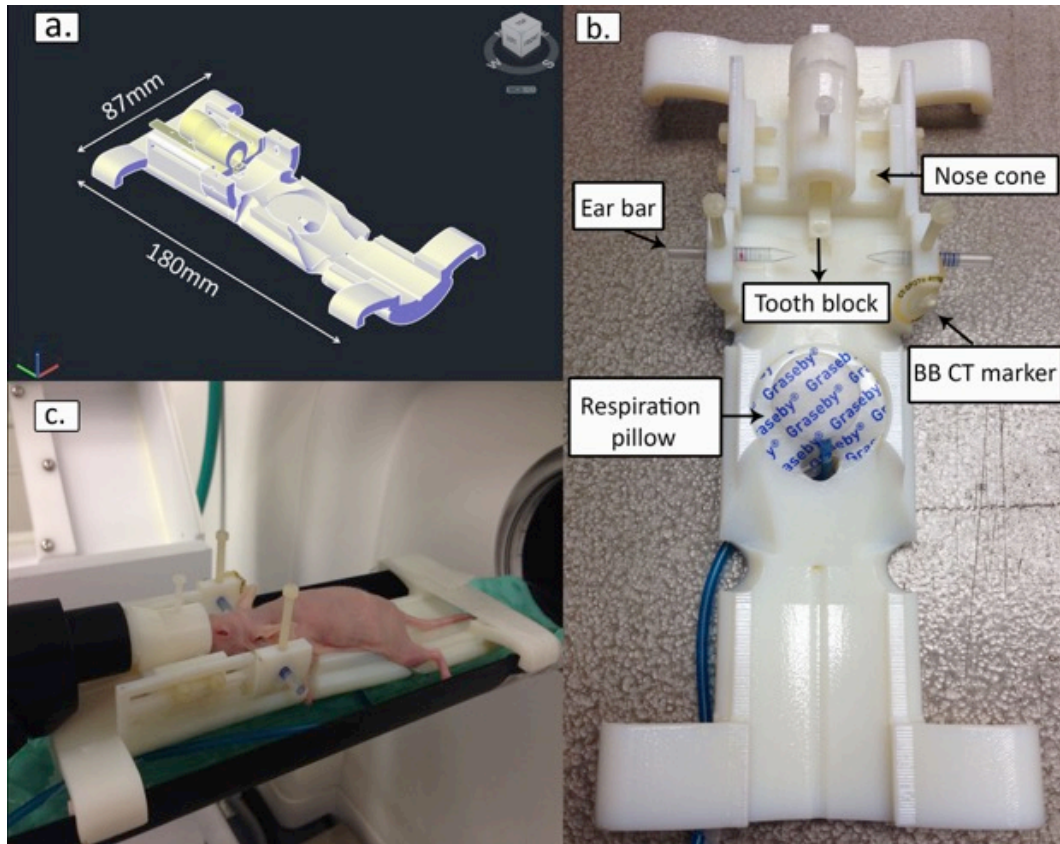


Figure 2-1: 3D-printed mouse head holder. a. Conceptual view of the head holder design in AutoCAD™ b. Photograph of 3D-printed holder with integrated respiratory monitoring pillow and adjustable nose cone, tooth bar and ear bars c. Mouse setup in head holder. A water blanket is used on top of the animal for thermal maintenance. A CT small ball bearing (BB) marker was placed on the right side of the head holder to help the user with the animal orientation on CT and fluoroscopy.

2.2.2 Mouse Brain Irradiation

All procedures followed animal care protocols approved by the Animal Use Subcommittee of The University of Western Ontario and were consistent with the policies of the Canadian Council on Animal Care (Appendix A: Animal Use Protocol). Mice were anesthetized using 1.5 to 2% vaporized inhaled isoflurane while held in the

3D-printed head holder (Figure 2-1c). Animals were placed in a feet first prone position inside the scanner. To validate targeting accuracy, the right half of brains from 10 adult mice (C57BL/6 or NU-Foxn1^{mu}) received the minimum dose of 16 Gy in a single fraction. Longitudinal fissure (LF) was determined as the anatomical target for the edge of the radiation field within the brain. Setup lasers were initially used to set the scanner landmark position relative to the head holder. CT images were used to verify the position of the ear bars and tooth bar (Figure 2-2a, b). Moreover, CT was used to check the mouse head alignment in 3D. Once the mouse was positioned for treatment, online dorsal-ventral fluoroscopy was acquired to identify the skull features and position the collimators. The collimators were moved so the animal body and left hemisphere of the brain were shielded. The right half of the brain was irradiated with a single field (14x20 mm²) from the animal's ventral-dorsal direction (Figure 2-3).

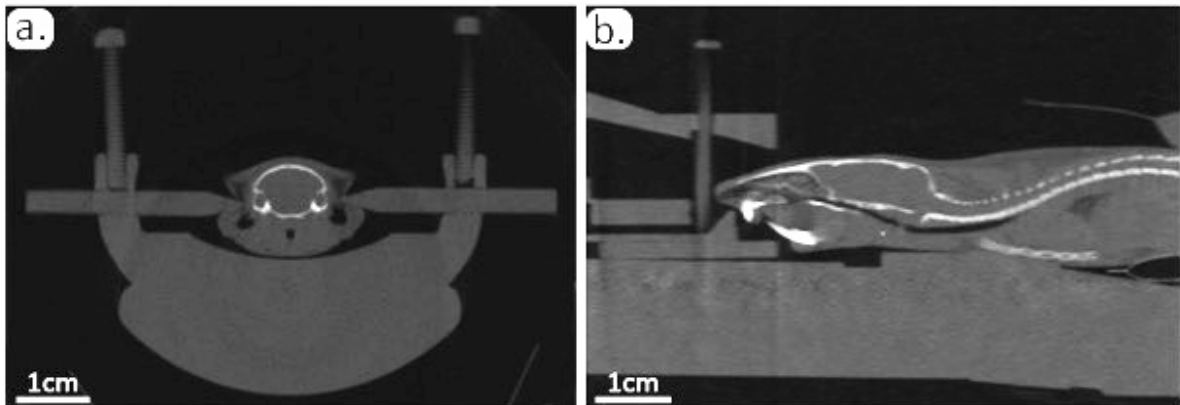


Figure 2-2: Pre-treatment CT images of the mouse brain positioned in 3D-printed head holder. a. Coronal view b. Sagittal view

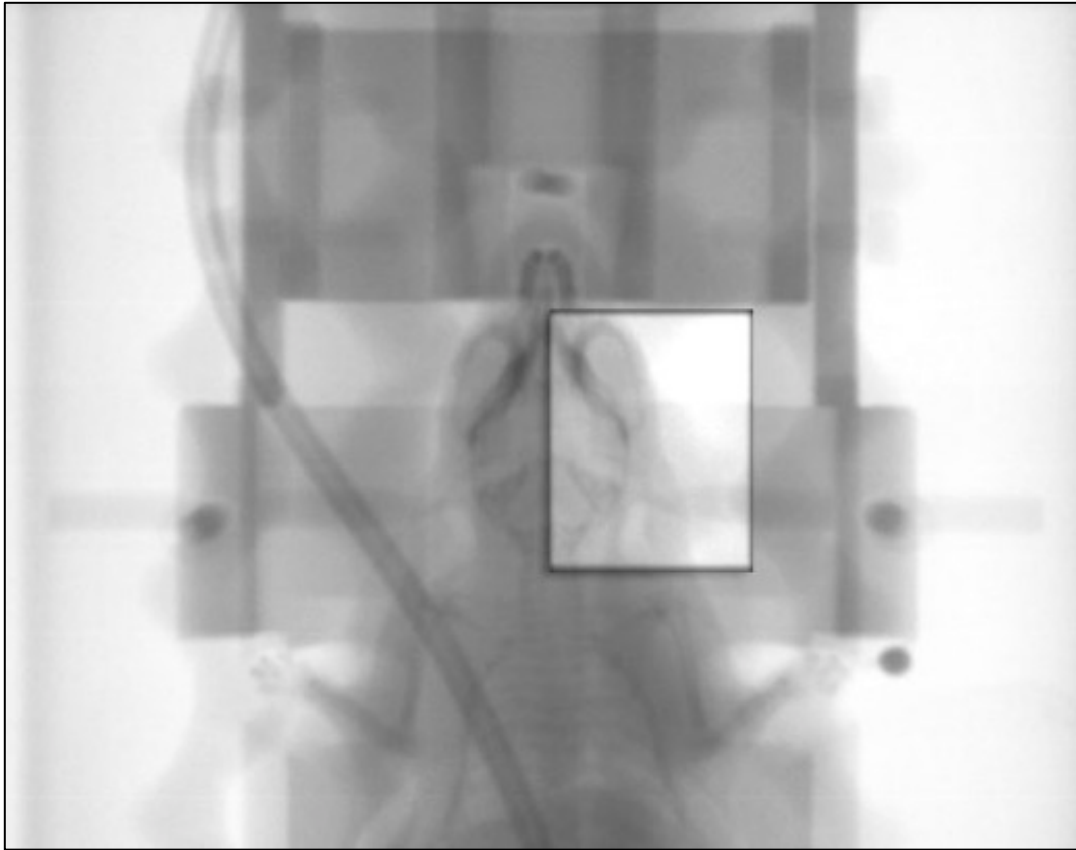


Figure 2-3: Beam's eye view fluoroscopy image of the mouse from the top (dorsal-ventral view). Animal is positioned prone in the 3D-printed head holder. The collimated radiation field ($14 \times 20 \text{ mm}^2$) is fused on top of the open field.

2.2.3 Immunohistochemistry

Mice were perfused with 0.9% saline containing 4% paraformaldehyde (PFA) approximately 30 minutes after treatment. Brains were harvested and post-fixed in 4% PFA followed by placing them in successive sucrose solution (10-30%) until the specimen sank to the bottom.^[14] Brain samples were embedded in Tissue-Tek OCT Compound (Sakura, Torrance, CA) and frozen. Cyrosectioning of coronal slices was performed with 10- μm slice thickness. Sections were stained for fluorescent γH2AX using a well-established protocol published by Ford *et al.*^[14]. Sections were stained with mouse anti- $\gamma\text{-H2AX}$ antibody (anti-phospho-histone H2AX, Ser139, clone JBW301;

Millipore, Billerica, MA, USA). DNA counterstaining was achieved with incubation in DAPI (4', 6-diamidino-2-phenylindole, Vector Laboratories, Inc. Burlingame, CA). A motorized fluorescence-scanning microscope (Leica Inc.) was used to automatically acquire images with a 10X objective and stitch them together to form whole brain images on stained histology sections of 5 mice. To quantify targeting accuracy, another set of 10X images, focusing on the midbrain region was acquired with a fluorescence microscope (Carl Zeiss Canada Ltd) for all 10 mice. All images were acquired under the same microscope settings and exposure parameters.

2.2.4 Analysis

Visualization of the actual beam in tissue was possible using γ -H2AX staining on *ex-vivo* brain sections. For targeting accuracy, we measured the distance from the edge of the radiation beam to the intended target (longitudinal fissure) using the digital readout of the fluorescent microscope (Figure 2-4 e). The edge of the radiation field was visually defined as the border separating cells having enhanced levels of γ -H2AX from those with background staining. The beam offset was measured on two separate histology samples for 8 of 10 mice, and only on one section from the remaining two mice (Figure 2-4 a-d). To measure the tilt of the animal's head around the rostral-caudal axis, the angle between longitudinal fissure and the γ -H2AX radiation border was determined on whole brain images in 5 mice.

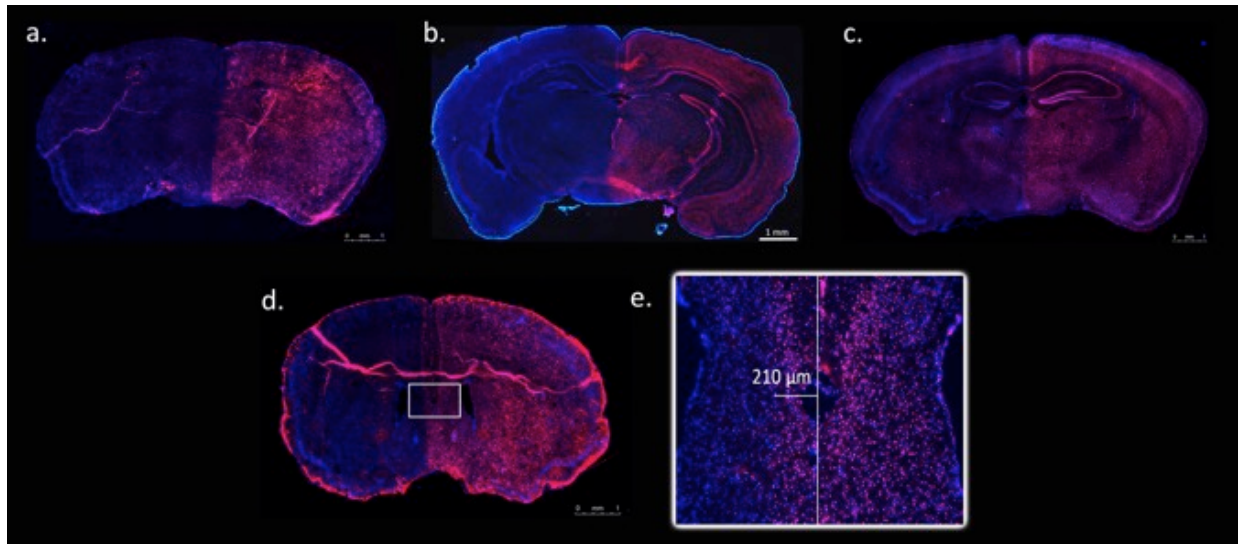


Figure 2-4: Fluorescence microscopy of γ -H2AX stained brain sections (red), imaged at 10X magnification. DAPI counterstaining of DNA is shown in blue. Sections from four irradiated mice treated in 3D-printed head holder are shown. Intended target was the right half of the brain. (a-d) Example measurement of targeting error on zoomed 10X image. Distance between longitudinal fissure (white line) and γ -H2AX field edge is shown (e).

2.3 Results

2.3.1 Mouse Set-up in 3D-printed Head Holder

Mice were under anesthesia for approximately two hours and breathing rate was monitored during treatment. Mice recovered well from isoflurane after treatment without any signs of trauma to their ears or mouth.

2.3.2 Validating Beam Targeting Accuracy with γ -H2AX Staining

Immunohistochemical staining of brain sections stained for γ -H2AX showed precise targeting of the field edge at the expected location. The sharp and straight edge of

the field through the whole brain for all samples indicates a stable and straight head position around the axis of gantry rotation. The edge of the beam was offset from the longitudinal fissure by a mean distance of $146 \pm 98\mu\text{m}$ (standard deviation) towards the left side in 10 mice. The average head tilt was determined to be $1.21 \pm 1^\circ$ (standard deviation) about the axis of the gantry rotation (rostral-caudal), indicating the x-ray source was positioned slightly towards the right side of the animal (Table 2-1).

Table 2-1: Targeting accuracy measurement of γ -H2AX stained brain sections. Positive angle indicates an x-ray tube towards the right side of the mouse. Positive offset indicates the radiation beam towards the left side of the longitudinal fissure.

Mouse	Tilt angle (degree)	Offset Measurement1 (μm)	Offset Measurement2 (μm)	Offset Mean (μm)
1	1.5	241	211	226
2	0.2	32	26	29
3	2.3	172	190	181
4	N/A	168	191	180
5	0.1	21	48	35
6	N/A	69	52	61
7	N/A	178	200	189
8	N/A	255	N/A	255
9	2.0	280	N/A	280
10	N/A	34	28	31

N/A indicates not available.

2.4 Discussion

We designed, implemented and verified a 3D-printed mouse head holder. With image guidance and the head holder, we found the radiation beam edge could be located within 0.15 mm of the intended target as determined by γ -H2AX immunohistochemical staining of mouse brain sections.

The 3D-printed head holder contains many of the desired features. Its fabrication is more economical than commercial versions and allows for modification according to specific experimental set-ups.

One possible limitation of 3D-printing is the strength of the material. To overcome the fragility of the material, the base of the head holder was designed thicker (1.5cm) compared to the other parts. Presence of the bed or ear bars in the path of the x-ray beam may interfere with dose delivery from lateral and ventral directions; therefore a different design may be needed for treating from other directions.

We validated our targeting accuracy by doing immunohistochemical staining of our samples. Physical changes such as tissue shrinkage and changes in morphology are possible during tissue processing. Wehrl *et al.*^[15] measured shrinkage between -11.7% to 30.7% for the PFA fixative depending on the anatomical landmark. Moreover, Ford *et al.*^[14] reported a shrinkage factor of 0.85 for fixed and frozen mouse brain samples. Applying the 0.85 shrinkage factor to our data, the mean beam offset is $172 \pm 115\mu\text{m}$.

The 3D-printed head holder assisted with animal positioning, however the beam offset from the target not only depends on the mouse head alignment, but also on the placement of the collimators. In this study, the half brain was determined visually using on-board imaging. Moreover, the 20%-80% radiation penumbra for $14 \times 20 \text{ mm}^2$ field is estimated to be 0.57-0.73mm for this system.^[2] All histological analyses were done on 10X microscope images, which is not suitable for detecting γ -H2AX foci in response to small doses. Only the sharp edge of the beam was detected and the localization may be dependent on microscope and display parameters.

Our designed 3D-printed mouse head holder may not only be applicable to mouse brain irradiation but potentially to other sites. With modification in design, our head holder may be a starting point for an even greater range of imaging and radiation preclinical studies.

2.5 Conclusions

Numerous studies have employed different stereotactic devices. We have demonstrated that a 3D-printed stereotactic head restraint can allow accurate and precise irradiation in a mouse brain. Immunohistochemical γ -H2AX staining validated the irradiation of specific sub-regions of the mouse brain with less than a millimeter error. Fast 3D-printing technology allowed us to produce a custom stereotactic holder with the necessary features for our study in an economical and timely manner.

2.6 Acknowledgment

We would like to thank John Moore for assistance in operating the 3D-printer. Frank Van Sas and Brian Dalrymple are acknowledged for assistance with post-printing fabrication. We thank Tom Hrinivich for helpful discussions and Heather Craig for assistance with the motorized microscope. This work is funded by the Natural Sciences and Engineering Research Council of Canada and London Regional Cancer Program Catalyst Grant and also supported by a Translational Breast Cancer Studentship award to NZ funded in part by the Breast Cancer Society of Canada.

2.7 References

1. DeSantis CE, Lin CC, Mariotto AB, Siegel RL, Stein KD, Kramer JL, et al. Cancer treatment and survivorship statistics, 2014. *CA Cancer J Clin* 2014;64(4):252–71.
2. Jensen MD, Hrinivich WT, Jung J a, Holdsworth DW, Drangova M, Chen J, et al. Implementation and commissioning of an integrated micro-CT/RT system with computerized independent jaw collimation. *Med Phys* 2013;40(8):0817061–08170613.
3. Tuli R, Armour M, Surmak a., Reyes J, Wong J. Abstract 5725: Accuracy of off-line bioluminescence imaging to localize targets in pre-clinical radiation research. *Cancer Res* 2012;72(4):5725–5725.
4. Van Hoof SJ, Granton P V., Verhaegen F. Development and validation of a treatment planning system for small animal radiotherapy: SmART-Plan. *Radiother Oncol* 2013;109(3):361–6.
5. Clarkson R, Lindsay PE, Ansell S, Wilson G, Jelveh S, Hill RP, et al. Characterization of image quality and image-guidance performance of a preclinical microirradiator. *Med Phys* 2011;38(2):845–56.
6. Dyk J Van, Battista JJ, Bauman GS. Accuracy and Uncertainty Considerations in Modern Radiation Oncology.
7. Baumann BC, Benci JL, Santoiemma PP, Chandrasekaran S, Hollander AB, Kao GD, et al. An Integrated Method for Reproducible and Accurate Image-Guided Stereotactic Cranial Irradiation of Brain Tumors Using the Small Animal Radiation Research Platform. *Transl Oncol* 2012;5(4):230–7.
8. Zhang L, Yuan H, Burk LM, Inscoe CR, Hadsell MJ, Chtcheprov P, et al. Image-guided microbeam irradiation to brain tumour bearing mice using a carbon nanotube x-ray source array. *Phys Med Biol* 2014;59(5):1283–303.

9. Kiehl EL, Stojadinovic S, Malinowski KT, Limbrick D, Jost SC, Garbow JR, et al. Feasibility of small animal cranial irradiation with the microRT system. *Med Phys* 2008;35(10):4735–43.
10. Holdsworth DW, Detombe S a., Chiodo C, Fricke ST, Drangova M. Implementation and assessment of an animal management system for small-animal micro-CT / micro-SPECT imaging David. *Proc SPIE* 2011;7965:79650N – 79650N – 6.
11. Pilch DR, Sedelnikova O a, Redon C, Celeste A, Nussenzweig A, Bonner WM. Characteristics of gamma-H2AX foci at DNA double-strand breaks sites. *Biochem Cell Biol* 2003;81:123–9.
12. Rogakou EP, Pilch DR, Orr AH, Ivanova VS, Bonner WM. DNA Double-stranded Breaks Induce Histone H2AX Phosphorylation on Serine 139. *J Biol Chem* 1998;273(10):5858–68.
13. Rothkamm K, Löbrich M. Evidence for a lack of DNA double-strand break repair in human cells exposed to very low x-ray doses. *Proc Natl Acad Sci U S A* 2003;100(9):5057–62.
14. Ford EC, Achantac P, Purgerc D, Armoura M, Reyesa J, J. Fonga L, et al. Localized CT-Guided Irradiation Inhibits Neurogenesis in Specific Regions of the Adult Mouse Brain. 2012;175(6):774–83.
15. Wehrl HF, Bezrukov I, Wiehr S, Lehnhoff M, Fuchs K, Mannheim JG, et al. Assessment of murine brain tissue shrinkage caused by different histological fixatives using magnetic resonance and computed tomography imaging. *Histol Histopathol* 2015;30(5):601–13.

Chapter 3

3 Evaluation of Radiation-Induced DNA Double-Stranded Breaks and Tumor Response in a Breast Cancer Brain Metastasis Model

This chapter is adapted from the manuscript entitled “ Evaluation of radiation-induced DNA double-stranded breaks and tumor response in a breast cancer brain metastasis model”. This research manuscript is in preparation and will be submitted to the *International Journal of Radiation Oncology * Biology * Physics* for publication. The authors of this manuscript are Zarghami N, Murrell DH, Jensen MD, Dick FA, Chambers AF, Foster PJ and Wong E.

3.1 Introduction

The improvement in survival rates in majority of primary cancers has led to an increase in the prevalence of brain metastasis. Each year, brain metastases are detected three to ten times more frequent than newly diagnosed primary malignant brain tumors, i.e. gliomas.^[1-3] The median survival of patients from the advent of brain metastasis is poor.^[4] Brain metastasis is associated with various types of disseminated cancer. The major primary sites include lung (40%-50%), breast (15%-25%) and melanoma (5%-20%).^[5-7] The unique micro-environmental structure of the brain often results in therapeutic failure with chemotherapy. Furthermore, brain is usually the last site of metastasis, after metastases to other visceral organs. Therefore, management of the brain metastasis is considered to be mainly palliative. Multiple brain metastases are often treated with the radiation dose of 30 Gy in 10 fractions using whole brain radiation therapy technique.^[8,9] Typically, patients with 1-3 lesions (each < 3 cm) are eligible for stereotactic radiation therapy alone or in combination with whole brain radiation therapy.^[7] The dose for stereotactic radiation of brain metastases varies, but most common prescription is 18-24 Gy in one fraction. While ionizing radiation (IR) is the

mainstay of treatment for these patients, in practice only one radiation scheme and schedule, such as described above, is employed for the treatment of all brain metastases.^[1,9,10] That is, despite the fact that the response of brain metastases to radiation therapy has been shown to depend on the type of primary tumor^[11,12], the same radiation scheme is prescribed for all brain metastasis.^[13]

The brain is a common metastasis site in breast cancer following bone and visceral organs. However, advances in adjuvant and chemotherapy drugs coupled with new sensitive imaging techniques have improved the control of extra-cranial diseases and unmasked brain metastasis as one of the late events in advanced breast cancer patients.^[14] The incidence of brain metastases in HER2+ and triple-negative is higher in comparison to other breast cancer subtypes.^[15,16] Patients with tripe-negative breast cancer are typically at higher risk of CNS relapse and have the poorest overall survival compared to other types as the treatment options are limited for this group.^[17] Brain lesions from breast cancer are heterogeneous. This heterogeneity is also reflected in their response to the treatment.^[18] Since the treatment for primary breast cancer is becoming more efficacious, the management of the metastasis from this disease should be re-examined. Understanding the response of breast cancer brain metastases to different radiation doses is essential for improving our knowledge and ultimately radiation dose prescription in clinics. Using sophisticated preclinical radiation therapy devices, imaging techniques and biological markers on breast cancer brain metastasis models, we are presented with a unique opportunity to reassess these fundamental yet critical radiobiology questions.

Radiotherapy relies on IR-induced DNA damage to control tumor cell division. DNA double-strand breaks (DSBs), are known to be lethal lesions that are responsible for the mitotic death from radiation.^[19] In response to IR-induced DSBs, histones H2A variant, H2AX, are rapidly phosphorylated to form γ -H2AX.^[20] γ -H2AX marker can be employed as an indirect measurement of DNA DSBs.^[21] It has been known that tumors have higher amount of “cryptogenic” γ -H2AX due to endogenous sources such as replication stress, genomic instability and uncapped telomeres compared to the healthy tissue.^[22-24] Timing is critical for γ -H2AX detection, as it decays over time. The time period of 30 to 60 minutes post exposure is often known to give reliable and maximal

scoring for radiation-induced damage.^[21] Depending on time-point after radiation exposure, γ -H2AX may also provide valuable information regarding DNA damage and repair kinetics. This technique has been used as a tool to predict the response to radiation and estimate the side effects in normal tissue after treatment.^[25,26] Studies have investigated the residual γ -H2AX of murine tissues from days to two months after exposure to detect radiation-induced toxicity such as fibrosis and myelopathy.^[27-29] These data prove the presence of DNA DSBs in some normal tissues long time after IR. To the best of our knowledge, no evaluation of residual γ -H2AX radiation response in breast cancer brain metastases has previously been examined.

The aim of this study was to evaluate the dose-response of human triple-negative breast cancer brain metastases to radiation, by irradiating half brain of MDA-MB-231-BR mouse model with various radiation doses. We assessed biological and morphological changes in tumors after radiation treatment. The histological radiation response was evaluated at two time points: 1) Acute (30 minutes after RT) and 2) Longitudinal (11 days after RT). Mice were also imaged with balanced steady state free precession (bSSFP) MR sequence before radiation therapy and 11 days after treatment. Changes in the volume of tumors were analyzed using MRI.

3.2 Material and Methods

3.2.1 Cell Culture

For this study, the brain tropic human triple-negative breast cancer cell line, MDA-MB-231-BR, stably transfected with enhanced green fluorescent protein (EGFP) was used.^[30] Cells were cultured and maintained in Dulbecco's modified eagle's medium (DMEM) containing 10% fetal bovine serum and 1% penicillin/streptomycin. Cultured cells were kept in 5% CO₂ at 37°C. Trypan blue exclusion assay was done to determine cell viability.

3.2.2 Animal Model

To deliver brain tropic MDA-MB-231-BR cells into the brain, intra-cardiac (IC) injection method was used to distribute cells through arterial circulation. Female nu/nu mice (N=18, 6–8 weeks old; Charles River Laboratories) were anesthetized with 1.5 to 2% vaporized inhaled isoflurane in O₂. A suspension containing 1.5x10⁵ MDA-MB-231-BR cells was slowly injected into the left ventricle of the beating heart of the mouse.^[31] This study followed animal care protocols approved by the Animal Use Subcommittee of The University of Western Ontario and were consistent with the policies of the Canadian Council on Animal Care (Appendix A: Animal Use Protocol).

Table 3-1: Irradiation group schedule for acute and longitudinal study. 0* = Un-irradiated half brain of the mice.

Study	Group	Number of Mice	Number of tumors on MRI	Dose (Gy)	Dissection after radiation therapy
Acute	A	3	>90	8	30 minutes
	B	3	>90	16	30 minutes
	C	4	>120	24	30 minutes
	D	8	>200	0*	30 minutes
Longitudinal	A	3	68	16	11 days
	B	2	34	24	11 days
	C	5	123	0*	11 days
	Control	3	10	0	11 days

3.2.3 *In-Vivo* MRI

All mice were imaged on a 3T GE Excite clinical MR scanner (General Electric, Mississauga, Canada) on day 26 after tumor injection. MRI was performed to verify the presence of the tumors in the mouse brain, particularly in both brain hemispheres. Images were acquired using 3D balanced steady-state free precession (bSSFP) protocol (Slice thickness = 200 μ m, resolution = 100 x 100 x 200 μ m, repetition time = 8 ms, echo time = 4 ms, flip angle = 35°, receive bandwidth = 19.23 kHz, signal averages = 2, radiofrequency phase cycles = 8, scan time = 29 minutes), a well-established imaging technique for this model by Foster *et al.*^[32-34] A small tube filled with vitamin E was used on the left side of the animal in the head coil to assist with the head orientation on MR images.

To evaluate the response of breast cancer brain metastases to different radiation doses *in-vivo*, the longitudinal group was imaged again 11 days after receiving half brain radiotherapy (37 days after injection). The same imaging protocol was used for post-radiotherapy MR image acquisition.

3.2.4 Mouse Hemi-Brain Irradiation

Mice received half brain radiation therapy on the modified GE eXplore CT 120 (GE Healthcare, Milwaukee, WI) preclinical imaging system.^[35,36] Mice were anesthetized using 1.5 to 2% vaporized inhaled isoflurane. All mice were immobilized using our customized 3D-printed head holder. We have previously demonstrated our targeting accuracy of < 0.15 mm using this system (see Chapter 2). Mice were set-up in feet first prone position. Longitudinal fissure (LF) was visually set as the anatomical target for the radiation field. Setup lasers and CT images were used to verify the alignment of the animal's head in the head holder. Once the mouse was set-up for treatment, online dorsal-ventral fluoroscopy was acquired to identify the rim of the skull and positioning the collimators. To target for focal half brain irradiation, the computerized collimators were moved, so the animal's body, the left hemisphere of the

brain and tumors within that side were shielded. A small ball bearing (BB) marker was placed on the right side of the head holder to help with animal orientation on CT and fluoroscopy. The right half of the brain was irradiated with a single field (14x20 mm²) from the animal's ventral-dorsal direction. Mice received doses of either 8, 16 or 24 Gy in a single fraction. When we assumed that $\alpha/\beta \sim 10$ Gy for the tumors, the calculated biological effective dose (BED) of 16 Gy and 24 Gy in a single fraction are equal to doses prescribed for whole brain radiation therapy and stereotactic radiosurgery in clinics respectively. Figure 3-1 shows a representative dose distribution in the mouse brain for a single fraction. The un-irradiated side of the brain and tumors within that half were denoted as the 0* and considered the control of the irradiated side in the same mouse. Mice recovered well from radiation and were selected either for acute or longitudinal dose-response study. Control (sham) cohort did not receive radiation nor CT scans and was the control of un-irradiated side.

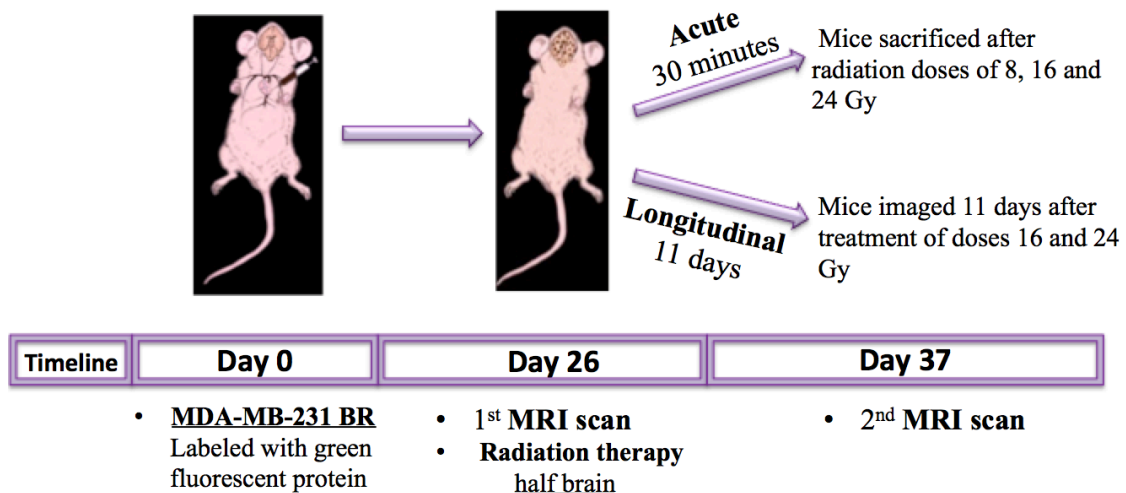


Figure 3-1: Radiation dose-response experimental design. Tumors (MDA-MB-231-BR) were injected on day 0. Twenty-six days after injection, all mice were imaged with MR and selected either for acute or longitudinal study. In the acute study, mice were scarified 30 minutes after receiving half brain radiotherapy. In the longitudinal cohort, mice were imaged 11 days after RT and were sacrificed.

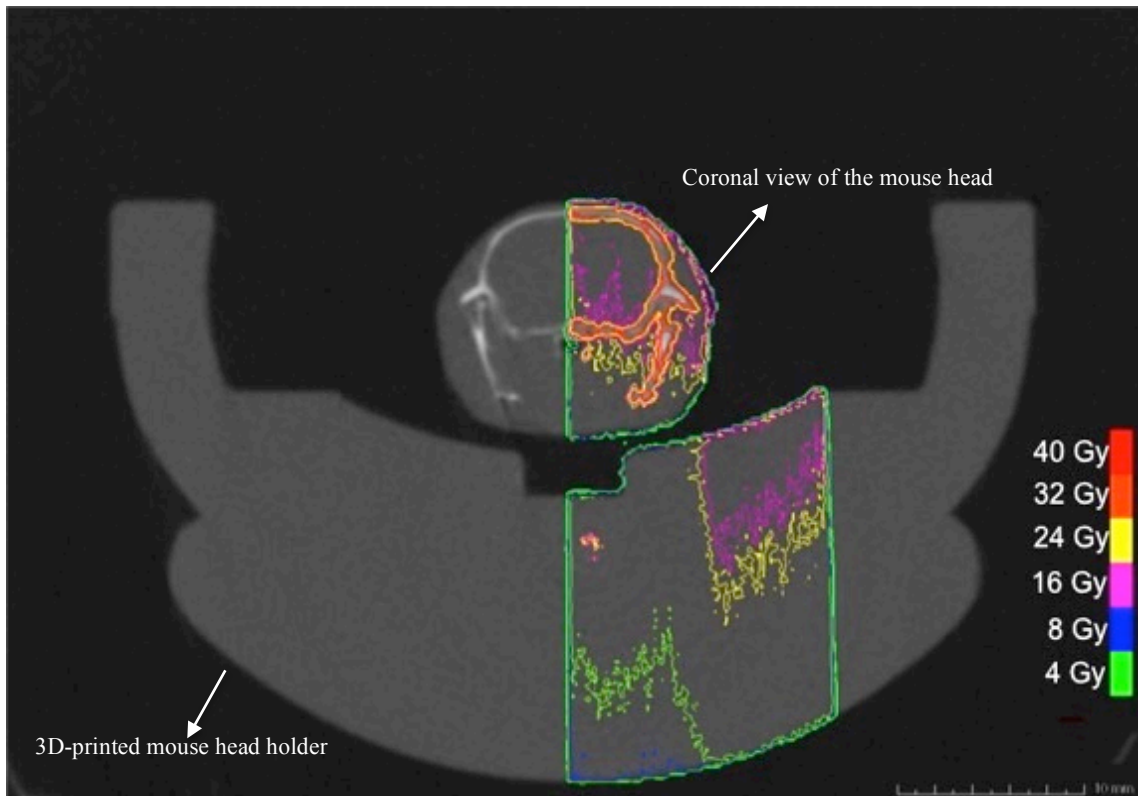


Figure 3-2: Calculated dose distribution on coronal CT plane of the mouse brain. Most of the right half of the brain received 16 Gy that matches with pink isodose line.

3.2.5 Immunohistochemistry

At the two post-irradiation time-points (30 minutes or 11 days) mouse brain samples were collected and processed for immunohistochemistry (IHC) staining. Mice were perfused with 0.9% saline followed by 4% paraformaldehyde (PFA). Brains were harvested, post-fixed in 4% PFA and transferred to 30% sucrose solution until the specimen sank to the bottom. Brain samples were embedded in Tissue-Tek OCT Compound (Sakura, Torrance, CA) and frozen. Cyrosectioning of coronal slices was performed with 10- μ m slice thickness. Tissue sections were stained with hematoxylin and eosin (H&E) to assess the morphology of the tumors.

Immunostaining was performed with the primary monoclonal antibody against γ -H2AX using a protocol published by Ford *et al.*^[37] Briefly, sections were incubated with mouse anti- γ -H2AX antibody (anti-phospho-histone H2AX, Ser139, clone JBW301; Millipore, Billerica, MA, USA) at the dilution of 1:700 at 4°C overnight and stained with secondary antibody Alexa-Fluoro 594 goat anti-mouse IgG (Life Technologies, Carlsbad, CA, USA) at the dilution of 1:500 for one hour at room temperature. DNA counterstaining was achieved with incubation in DAPI (4', 6-diamidino-2-phenylindole) and sections were mounted with anti-fade mounting medium Vectashield (Vector Laboratories, Inc. Burlington, ON). Detailed staining protocol is described in Appendix B. This protocol was used consistently to stain sections from the two time-points. For quantification, images were acquired with 100X (oil immersion) objective lens on a fluorescence microscope (Carl Zeiss Canada Ltd). Imaging acquisition parameters such as intensity, exposure time and gain were kept consistent during the experiment. We collected a total of ten to thirteen images of different tumors for each mouse.

3.2.6 Histological Quantification

To evaluate the DNA damage response, γ -H2AX stained sections of tumors were analyzed for each radiation dose. The amount of damage was also quantified in neighboring normal brain tissue that were treated under the same condition as tumors. The common approach for γ -H2AX quantification is scoring foci in the nuclei using high-resolution 3D images acquired from the confocal microscope.^[38] Initially, we employed this method and acquired images from the inverted confocal microscope (Olympus Fluoview FV1000 Confocal Imaging System). Figure 3-2 shows the images from irradiated tumors for both acute and longitudinal studies. We observed in the acute setting γ -H2AX foci were over-lapping, especially for high radiation doses, which made detection of individual foci impossible. Similarly, foci saturation was observed in some of the irradiated tumors in the longitudinal experiment. Unable to count individual foci, we quantified γ -H2AX based on the fluorescent stain intensity, which is a more reliable method for high radiation doses.^[39,40]

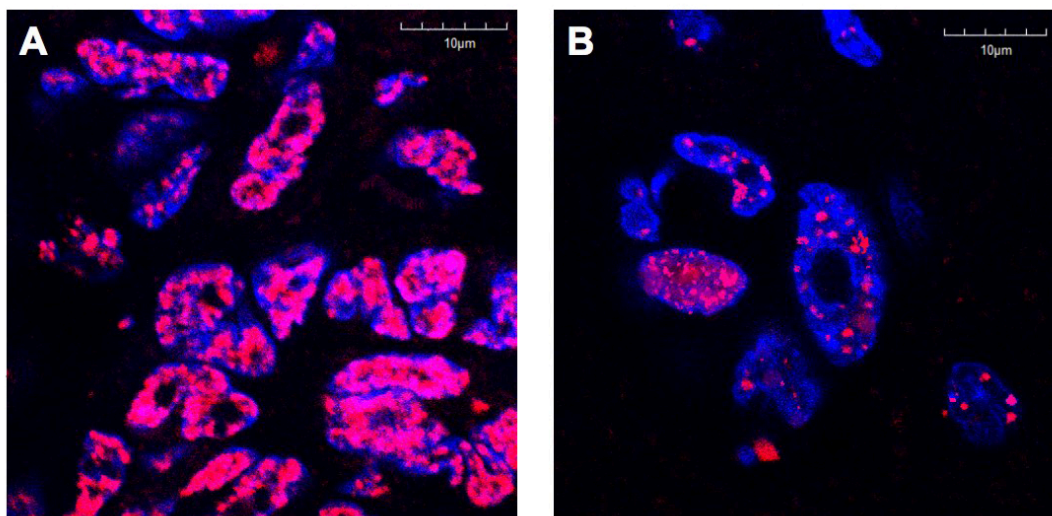


Figure 3-3: Merged DAPI and γ -H2AX tumor sections taken from the confocal microscope. (Blue=DAPI, Red= γ -H2AX) A: 30 minutes after irradiating tumors with 16 Gy. Discrete foci were not distinguishable in the acute experiment. B: 11 days after irradiating tumors with 16 Gy. Overlapping foci were also detected in some of the irradiated tumors nuclei.

All IHC analyses were performed on images taken from fluorescence microscope using 100X oil immersion objective. The γ -H2AX intensity was measured for both mouse normal brain and tumor tissues. Tumor nuclei were distinguished from mouse nuclei based on characteristic punctuate pattern of mouse DAPI staining.^[41] To quantify γ -H2AX intensity, DAPI-stained nuclei were used to generate nuclear outlines in which the γ -H2AX intensity would be measured. Nuclear segmentations were used to eliminate signal from background fluorescence. Nuclei on DAPI images were manually segmented using Adobe Photoshop CC. For each field of view, total γ -H2AX fluorescence intensity was automatically obtained by summing the values of all pixels within the segmented boundary using an in-house code developed in MATLAB (MathWorks, Natick, MA, USA). The total γ -H2AX fluorescence intensity for each field of view was normalized to the total area of segmented nuclei for the same field (Equation 3-1):

$$\gamma\text{-H2AX fluorescence intensity per unit area} = \frac{\text{Total } \gamma\text{-H2AX intensity in segmented nuclei}}{\text{Total area of segmented nuclei}} \quad (3-1)$$

Mean γ -H2AX intensity per unit area was determined for each treatment condition. The total number of nuclei analyzed for each dose level varied from 350 to 950. Moreover, we assessed the size of tumor nuclei by computing the average area of each nucleus from DAPI images (Equation 3-2):

$$\text{Average area per tumor nucleus} = \frac{\text{Total area of segmented nuclei}}{\text{Number of segmented nuclei}} \quad (3-2)$$

We observed that MDA-MB-231-BR tumors grew in clusters surrounded by edema. We obtained number of tumor nuclei per cluster area. This index gave us the density of tumor nuclei/cells in each cluster (Equation 3-3):

$$\text{Tumor cell density} = \frac{\text{Number of tumor nuclei in cluster}}{\text{Area of segmented cluster}} \quad (3-3)$$

We quantified both the tumor cell density and size of tumor nucleus for all radiation doses at the two time-points. Figure 3-3 shows the flow chart of the processes involved in these histological quantifications. IHC staining was repeated three times for the acute study and twice for the longitudinal study. Quantitative analyses of the latest set of stains will be presented.

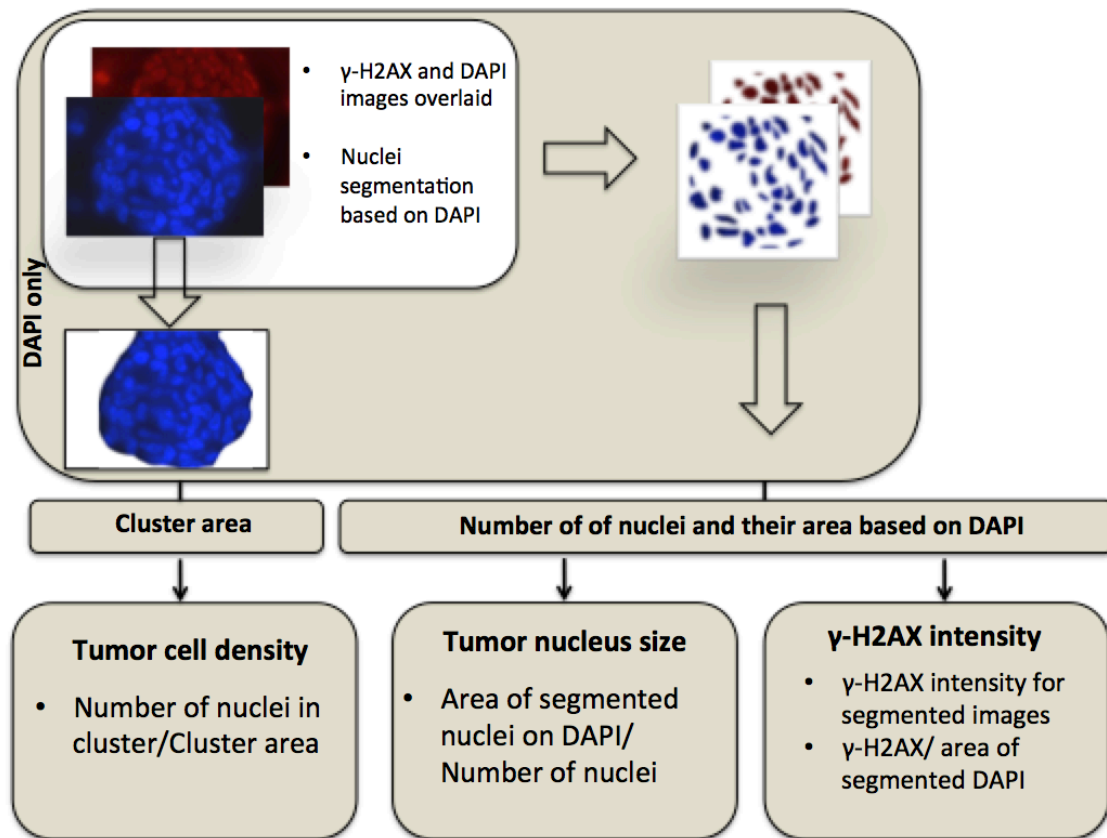


Figure 3-4: Flow chart of the processes involved in the quantification of γ -H2AX intensity, tumor nucleus size and tumor cell density. DAPI and γ -H2AX images were overlaid and nuclei were segmented based on DAPI. From the segmented DAPI images, number and total area of segmented nuclei were quantified. The intensity of γ -H2AX from segmented nuclei was acquired. For tumor cell density analysis, tumor clusters were segmented based on DAPI and the area of the cluster was computed.

3.2.7 MRI Analysis

Brain metastases were segmented manually on pre and post-radiotherapy images by a single observer using open-source OsiriX image software version 6.0. Tumors in the midline of the brain ($\pm 200 \mu\text{m}$ of the longitudinal fissure) were excluded from the study as only part of the tumors may be irradiated and part not. To determine the response of brain metastasis to radiation therapy on MR images, the mean fractional volume changes of the tumors were calculated. This index was calculated by dividing the tumor volume (mm^3) 11 days after treatment by the volume of the same tumor before treatment and averaged for all brain metastasis for mice in each group.

3.2.8 Statistics

Statistical analyses were performed using SPSS (Armonk, NY: IBM Corp) and confirmed by GraphPad Prism (La Jolla, CA, USA) software. Between-groups analysis of variance (ANOVA) followed by Tukey *post-hoc* test was conducted to determine whether the response was statistically significant ($p < 0.05$) between radiation dose levels for both *ex-vivo* and *in-vivo* studies.

3.3 Results

3.3.1 γ -H2AX Radiation Dose-response

Formation of γ -H2AX in the nuclei of cells is one of the primary responses to radiation-induced DNA DSBs. In the acute radiation dose-response study, mice received half brain radiation of 8, 16 and 24 Gy (minimum $N=3$ per dose) and were sacrificed approximately 30 minutes after treatment. Histology sections were stained for γ -H2AX to quantify the initial damage induced in both normal brain and tumors. Figure 3-4 displays mouse whole brain coronal section, which received half brain radiation of 16 Gy.

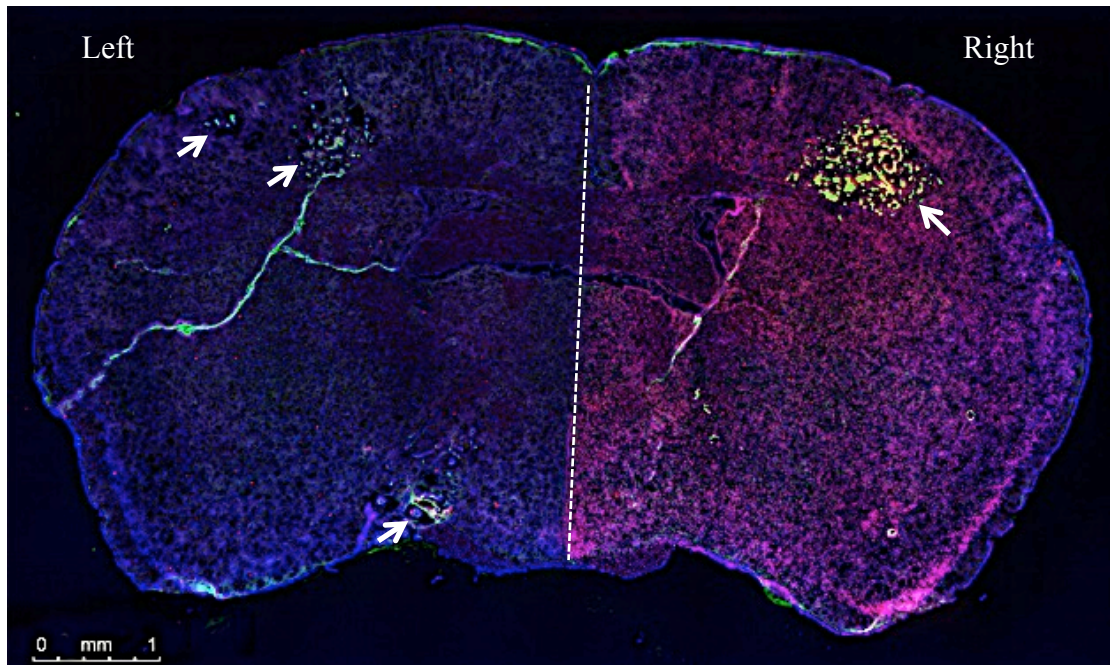


Figure 3-5: Whole brain image of γ -H2AX stained brain section (red), imaged at 10X. DAPI counterstaining of DNA is shown in blue. Stable EGFP labeled tumors are in green (white arrows). The intended target was the right half of the brain. White dashed line shows longitudinal fissure, the anatomical radiation target. γ -H2AX stain shows the sharp edge of the beam in the middle of the brain and demonstrates the tumor on the right side is irradiated while the ones on the left are spared.

Figure 3-5 shows the histology sections of tumors and normal brain tissue stained with DAPI and γ -H2AX for the acute study.

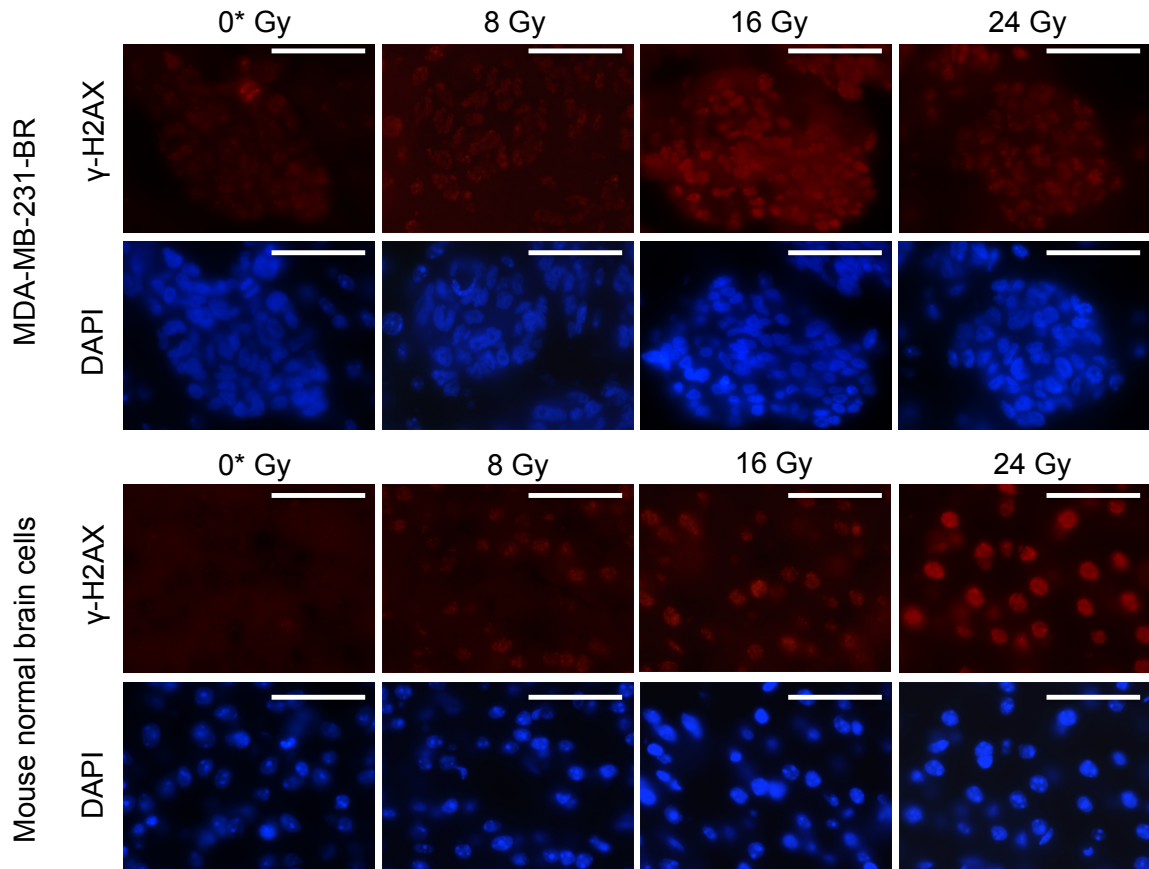


Figure 3-6: Initial DNA damage response 30 minutes post-irradiation. Histology sections of fluorescent γ -H2AX and corresponding DAPI (nuclei) stained for tumor (MDA-MB-231-BR) and normal brain are shown. Images were taken with the fluorescence microscope (100X objective) Scale bar=50 μ m

In general, the γ -H2AX images exhibited increasing intensity with radiation dose. Figure 3-6 shows the quantification of γ -H2AX based on fluorescence intensity in normal brain and tumor tissues. In normal brain, the amount of γ -H2AX intensity increased linearly ($R^2= 0.78$, $p <0.001$) with increasing radiation dose. However, in tumors this trend stopped at 16 Gy and the level of γ -H2AX intensity dropped for the dose of 24 Gy. The γ -H2AX intensity between irradiated and un-irradiated sides was significantly different in both tumors and normal brain.

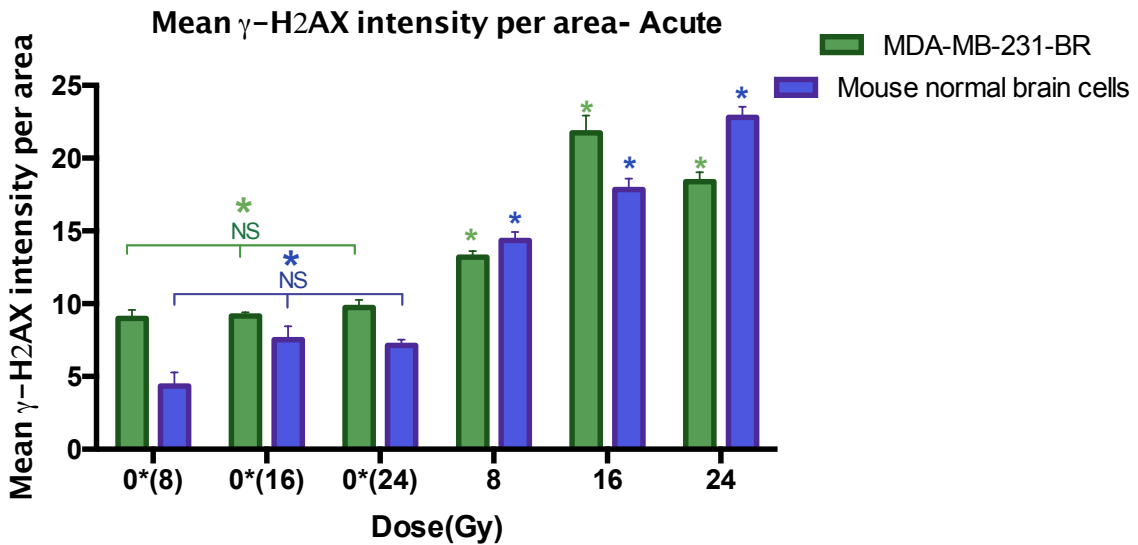


Figure 3-7: Quantification of the intensity of γ -H2AX staining versus radiation dose 30 minutes after radiotherapy. Green bars indicate tumors and blue bars are neighboring normal brain tissue. In normal brain nuclei, the γ -H2AX intensity was significantly different for all radiation doses and had a linear trend. In tumors, γ -H2AX dropped down for the dose of 24Gy. $*= p \leq 0.05$, Error bar = standard error of the mean

To evaluate the amount of residual γ -H2AX 11 days after hemi-brain radiation, and to investigate how much of the initial damage is retained in both tumors and normal brain tissues, γ -H2AX intensity was measured for longitudinal group (Figures 3-7, 3-8).

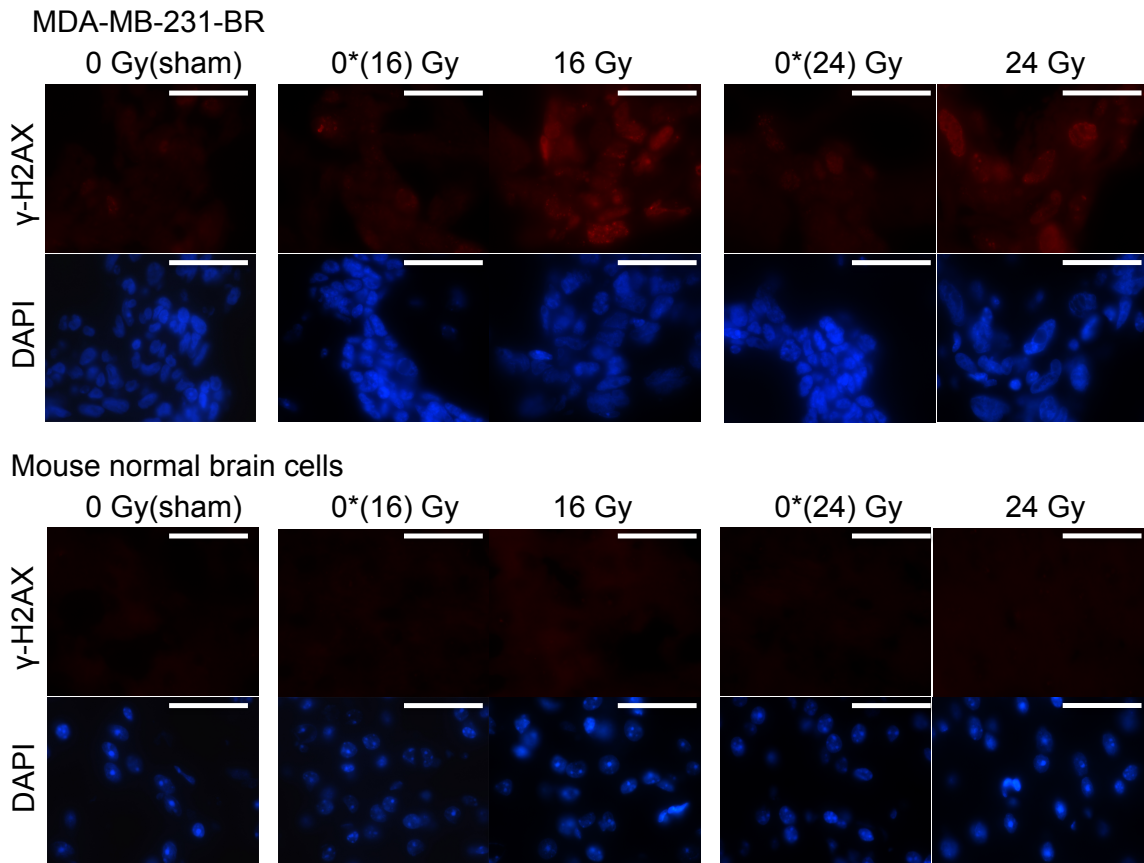


Figure 3-8: Residual DNA damage response 11 days post-irradiation. Histology sections of fluorescent γ -H2AX and corresponding DAPI (nuclei) staining for MDA-MB-231-BR and normal brain are shown. Images were taken with the fluorescence microscope (100X objective) Scale bar=50 μ m

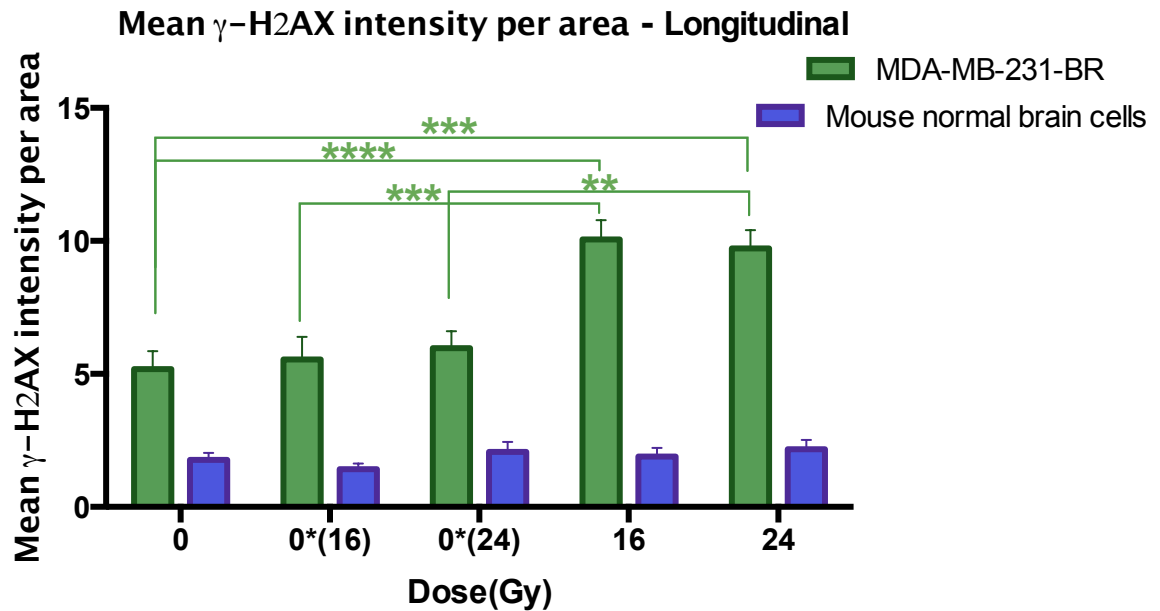


Figure 3-9: Quantification of the intensity of γ -H2AX staining for the various radiation dose 11 days after radiotherapy. Green bars indicate tumors and blue bars are neighboring normal brain tissue. In normal brain, γ -H2AX intensity decreased to the background level. In irradiated tumors, γ -H2AX intensity was higher than both the background level and tumors in the un-irradiated side. **= $p \leq 0.01$, *= $p \leq 0.001$, ****= $p \leq 0.0001$, Error bar= standard error of the mean**

We observed that the amount of γ -H2AX returned to the background level in irradiated normal brain nuclei 11 days after radiotherapy but not in the irradiated tumors. There was no significant difference in the amount of residual γ -H2AX between irradiated tumors (16 Gy vs. 24 Gy). However, irradiated tumors had higher levels of γ -H2AX compared to tumors in the contralateral un-irradiated sides (0*(16) and 0*(24) Gy).

3.3.2 Tumor Cell Nuclear Size

The DAPI stain binds to A-T base pairs and is used as a counterstain for the chromosome and nucleus of the cell. For this reason, we used this stain to investigate the size of tumor nuclei for both acute and longitudinal studies. We observed that the nuclei of treated tumors were significantly larger than the un-treated nuclei 11 days after radiotherapy. Figure 3-9 shows the different morphological appearances of irradiated versus un-irradiated tumor nuclei stained with DAPI.

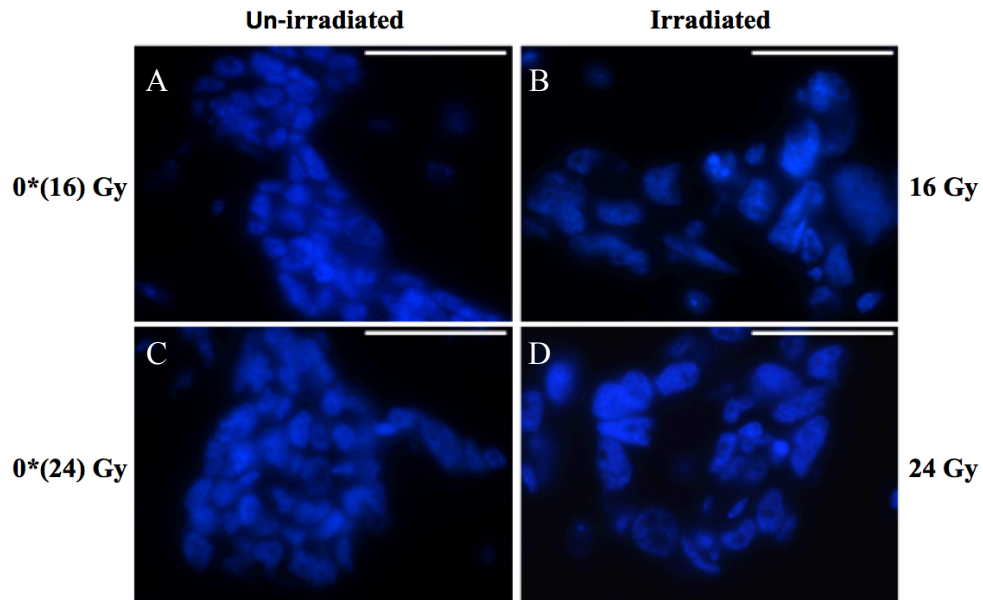


Figure 3-10: DAPI staining of tumor nuclei 11 days after radiotherapy. (A, B): Tumors in the same section of the mouse brain, A: Un-irradiated side, B: Irradiated with 16 Gy. (C, D): Tumors in the same section of the mouse brain, C: Un-irradiated side, D: Irradiated with 24 Gy. 100X magnification. Scale bar=50 μ m

The size of tumor nuclei was quantified for both acute and longitudinal studies. The acute setting quantification was employed to establish a baseline. Figure 3-10 shows the average size of tumor nuclei 30 minutes after treatment. No significant difference was found between groups. However, in the longitudinal cohort, there was a significant difference in the size of the nuclei between treated and un-treated side of the same mice and between two radiation doses of 16 and 24 Gy (Figure 3-11).

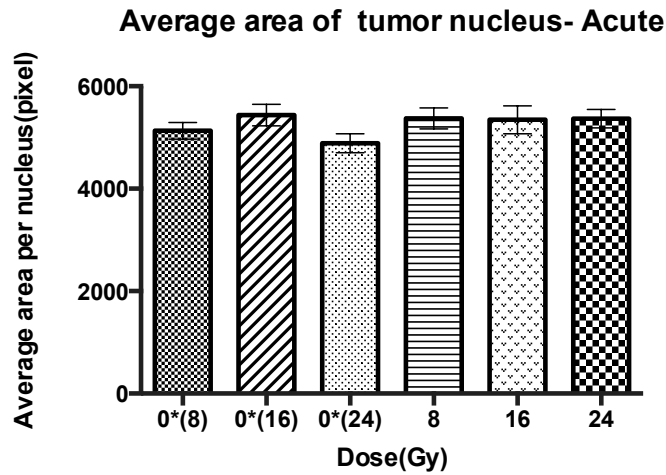


Figure 3-11: Average size of tumor nuclei 30 minutes after radiotherapy. No significant difference was found between groups. Error bar= standard error of the mean

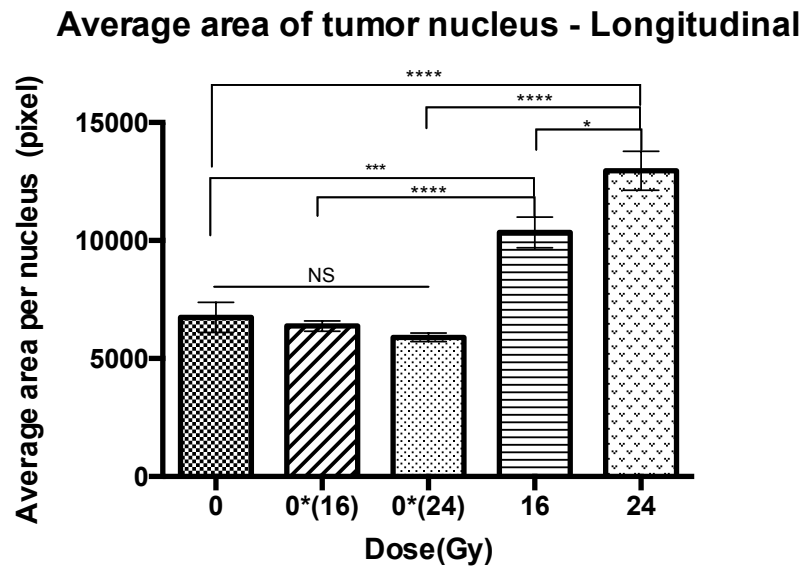


Figure 3-12: Average size of tumor nuclei 11 days after radiotherapy. There was a significant difference between the size of tumor nuclei treated with 16 Gy versus their contralateral side. The same significance was seen for the dose of 24 Gy. The amount of radiation dose also played a significant role in the size of tumor nuclei between 16 and 24 Gy. No significance (NS) was found between un-irradiated sides of the two doses and the sham group. $* = p \leq 0.05$, $*** = p \leq 0.001$, $**** = p \leq 0.0001$, Error bar= standard error of mean

3.3.3 Tumor Cell Density

We observed on H&E samples from the longitudinal cohort that irradiated tumor clusters are less compact, and surrounded by more substantial amount of edema compared to tumor clusters on the un-irradiated side (Figure 3-12).

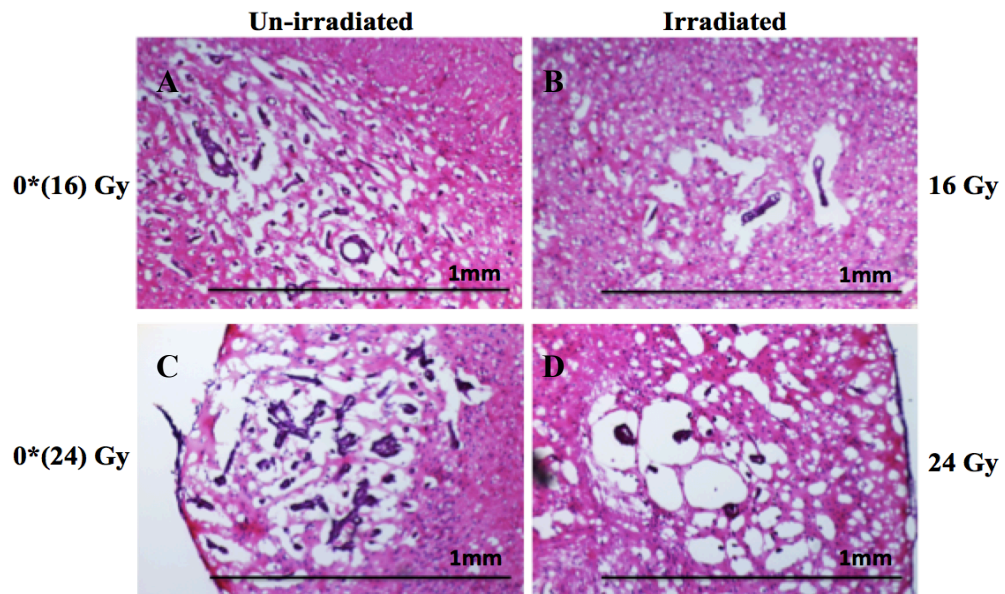


Figure 3-13: H&E stained sections of tumors 11 days after radiotherapy. (A, B): Tumors in the same section of the mouse brain, A: Un-irradiated side, B: Irradiated with 16 Gy. (C, D): Tumors in the same section of the mouse brain, C: Un-irradiated side, D: Irradiated with 24 Gy. 10X magnification.

In order to quantify this histological observation, we calculated tumor cell density based on DAPI staining. We measured this index for both acute and longitudinal settings in tumors. Figure 3-13 shows the tumor cell density on day 26. No significant difference was detected in the density between treated and un-treated tumors and different radiation doses 30 minutes after radiation therapy.

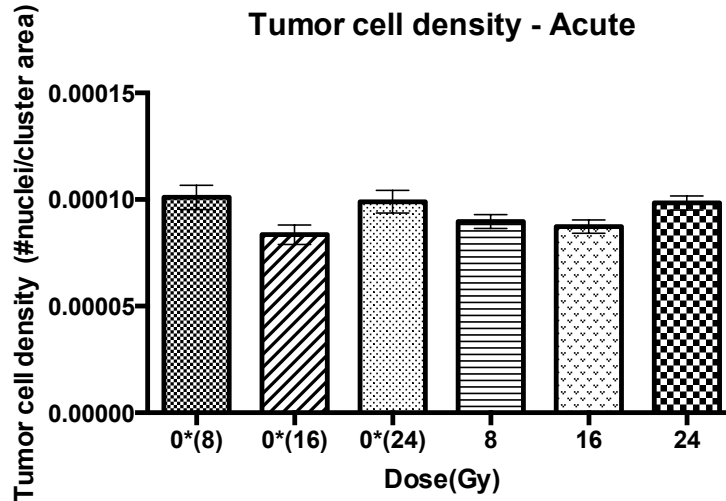


Figure 3-14: The tumor cell density 30 minutes after radiotherapy. No significant difference was found between the irradiated and un-irradiated groups. Error bar= standard error of the mean

On the other hand, we found a significant difference between treated and un-treated tumors in the longitudinal experiment. Figure 3-14 plots the average tumor cell densities 11 days after radiotherapy. These results suggest that the population of tumor nuclei per area of a cluster significantly decreased after radiotherapy. Histology samples of $n \geq 2$ mice were analyzed for each group. Furthermore, when we compare tumor cell density between longitudinal irradiated and that in the acute setting, we found that at 16 and 24 Gy, the tumor density at day 11 is about half that of the acute settings.

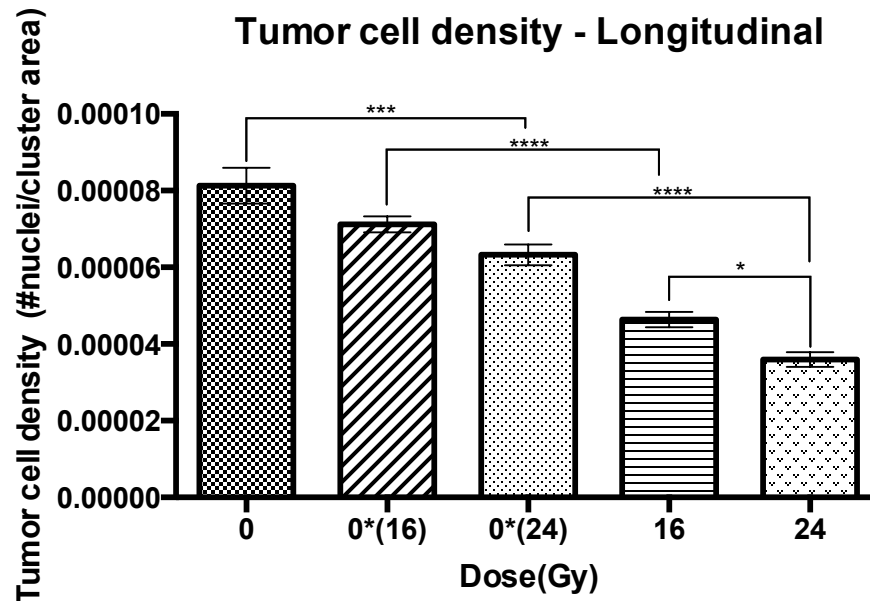


Figure 3-15: The tumor cell density 11 days after radiotherapy. The density for tumors treated with 24 Gy was lower than other groups and significant with the un-treated side. The same significant difference was found between tumors treated with 16 Gy and the un-treated side. There was a significant difference between treated tumors. No significance was observed between the tumor cell density of control (sham) and un-irradiated side of 16 Gy. *= $p \leq 0.05$, ***= $p \leq 0.001$, ****= $p \leq 0.0001$, Error bar= standard error of the mean

3.3.4 *In-vivo* Dose-Response

To assess the changes in the volume of tumors in response to radiation doses *in- vivo*, MR images were taken before and 11 days after half brain radiation therapy. Representative images of brain metastases at two different time-points for doses of 16 and 24 Gy and control (sham) are shown (Figure 3-15).

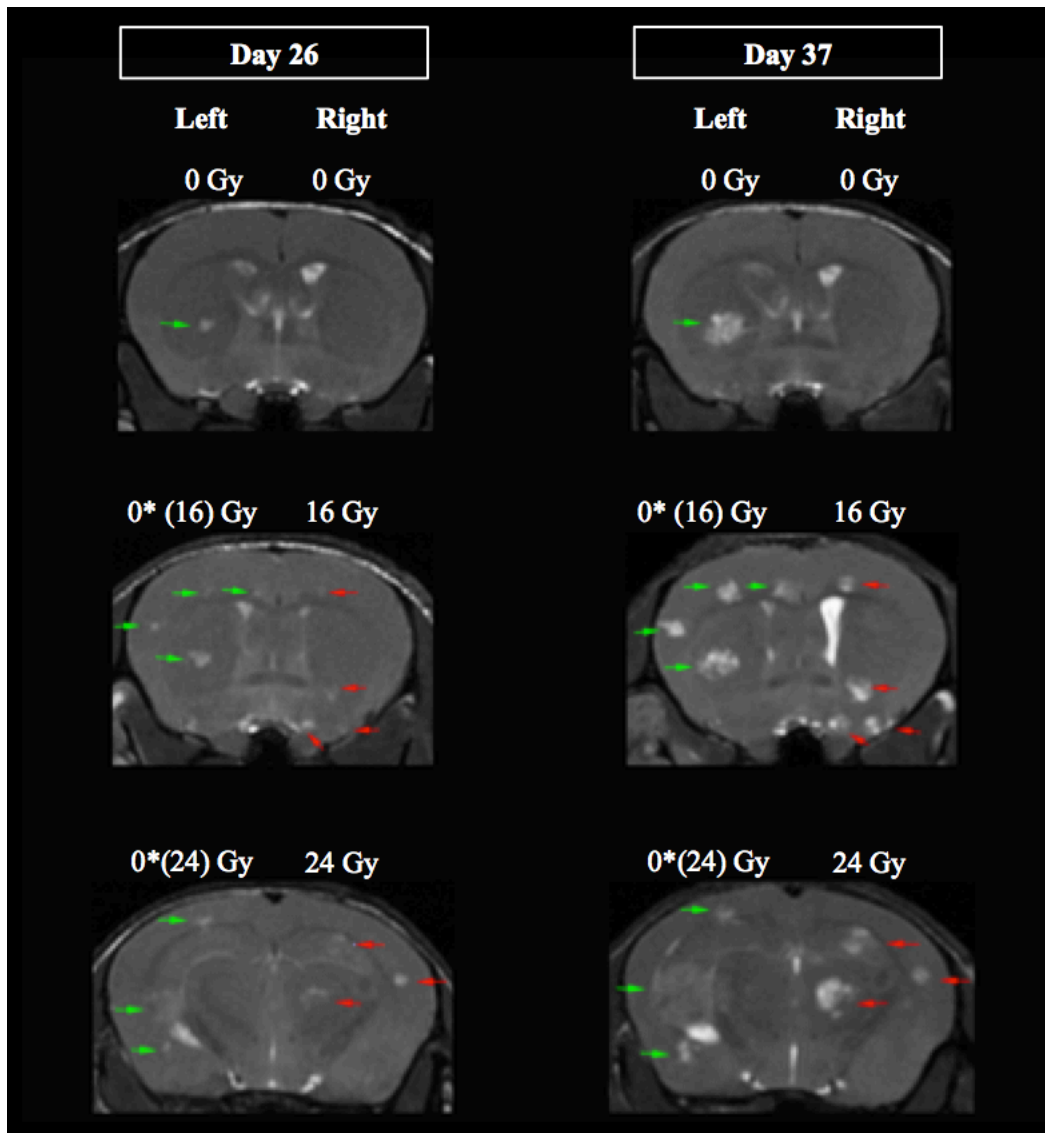


Figure 3-16: MR images (bSSFP) of the mouse brain at two-time points. Metastases appear as hyper-intense (bright) regions compared to brain parenchyma. Day 26 shows pre-treatment images and day 37 is 11 days after radiation therapy for the same mouse. Right half of the brain was irradiated. One mouse per group is shown. Red arrows indicate the brain metastases in the irradiated side (i.e. received radiation) while green arrows show brain metastases in the un-irradiated side.

The tumor segmentation on MR images at the end-point of the longitudinal study revealed that the tumor volume increased whether they received radiation or not. The mean fractional growth of the tumors was calculated for each group (Figure 3-16). There was a statistically significant difference between the growth of un-irradiated 0*(16 Gy) and irradiated brain metastases for dose of 16 Gy. While there was a trend, no significant difference in the fractional growth on MR was found for dose of 24 Gy and tumors in their counterparts 0*(24 Gy) and between the treated tumors at 16 and 24 Gy. Lastly, we found a significant difference between 0 (sham) and un-irradiated sides 0*(16 and 24 Gy).

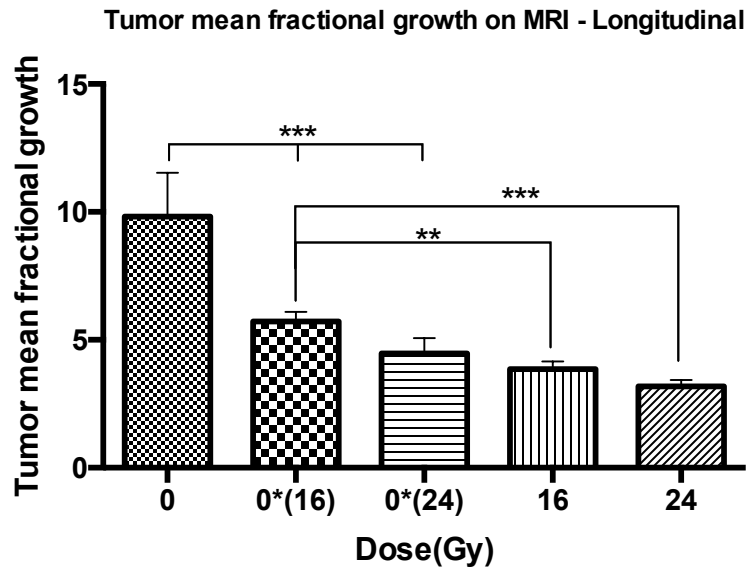


Figure 3-17: The mean fractional growth of brain metastases measured on MR images for various radiation doses. On average tumors in the sham cohort and un-irradiated sides 0*(16) and 0*(24) Gy grew 9.5 ± 1.5 , 5.7 ± 0.3 and 4.4 ± 0.5 (std. error of mean) times respectively. Tumors that received doses of 16 or 24 Gy grew by a factor of 3.8 ± 0.3 and 3.1 ± 0.25 (std. error of mean) respectively. There was a significant difference between the growth of tumors irradiated with 16 Gy versus their un-irradiated side. MRI detected no significant difference between the growth of 16 and 24 Gy treated tumors longitudinally. A significant difference was observed between sham group and tumors in un-irradiated sides. **= $p \leq 0.01$, *= $p \leq 0.001$, Error bar= standard error of the mean**

3.4 Discussion

In this study, we evaluated the response of triple-negative breast cancer brain metastases to different radiation doses both *ex-vivo* and *in-vivo* at two time-points after treatment.

In the acute experiment, mice were sacrificed 30 minutes after receiving radiation doses of 8, 16 and 24 Gy. γ -H2AX was used as a marker to measure the amount of induced DNA DSBs. The IR damages in normal brain and tumor cells were quantified for each dose level and compared to the un-irradiated side. Previous studies have reported a linear relationship between radiation dose and γ -H2AX foci number and/or relative fluorescence intensity up to lethal dose of 100 Gy.^[21,42] We showed that the amount of damage detected by γ -H2AX fluorescence intensity indeed has a linear correlation with radiation dose ($R^2=0.78$, $p<0.001$) in normal brain nuclei. On the contrary, this trend was not observed in tumors. For the dose of 24 Gy in a single fraction, the amount of γ -H2AX fluorescence intensity in tumors adjacent to normal brain tissue decreased. The γ -H2AX saturation has been reported in dose-response experiments on tumor cell lines *in-vitro* for high radiation doses.^[43] One reason for the γ -H2AX reduction for the dose of 24 Gy may be due to the micro-CT/RT dose rate. The dose rate used for this experiment was approximately 0.2 Gy/minute and it took about 2 hours to deliver 24 Gy. The γ -H2AX level is correlated with the dose rate, and it reaches a plateau if the cells get to the damage-repair equilibrium state.^[44,45] Moreover, the fact that γ -H2AX measures DNA DSBs indirectly may also contribute to this observation. γ -H2AX acts as an amplifier to recruit DNA damage response machinery immediately after the radiation insult and does not necessarily show true physical DNA breaks.^[46,47] Once the repair mechanism has been activated, phosphorylation of more H2AX is not critical.^[48] Interpreting our findings according to this perspective, the initial radiation-induced phosphorylation of H2AX was sufficient for repair mechanism activation and recruitment in irradiated tumors. Unlike normal brain tissues, further radiation insults in tumors did not result in phosphorylation of new H2AX protein implying a difference in the feedback mechanism of DSB repair and sensing between normal mouse brain tissues and tumors. Similar results were also observed by Mariotti *et al.*^[48] They reported that the number of γ -H2AX foci delivered

with 5 hours gap or more did not increase.^[48] Indeed, reduced γ -H2AX intensity does not necessarily mean less damage to the tumors for the dose of 24 Gy versus 16 Gy.

In the longitudinal experiment, tumor models received hemi-brain radiation doses of 16 and 24 Gy. We scanned them 11 days after treatment to detect changes in tumors on MRI and histology.

Our longitudinal γ -H2AX results showed that in normal brain nuclei the γ -H2AX level returns to the background level. However, irradiated tumors retained their higher amount of γ -H2AX compared to the background and un-irradiated tumors 11 days after radiotherapy. It has been shown that tumors that retain the induced γ -H2AX in the first 24 hours after radiotherapy are more likely to die.^[49] To the best of our knowledge, this is the first study to evaluate tumors' residual γ -H2AX on histological samples longitudinally. However, the time span of 11 days is sufficient for the damaged tumor cells to die and be removed. We hypothesize that the remaining tumor cells are surviving (positive for Ki-67, data not shown) but with higher residual γ -H2AX. We speculate the remaining irradiated tumors have unstable genome due to their defective repair mechanism and/or mutations induced after radiotherapy. Indeed, it has been shown that tumors have an excessive amount of γ -H2AX.^[24] There are a number of explanations for high cryptogenic level of γ -H2AX in tumor cells such as dysfunctional telomeres, which provides a signal for γ -H2AX and drives genomic instability.^[50] Yu and colleagues have also shown higher endogenous levels of γ -H2AX in the more aggressive and heterogeneous tumor cell lines.^[51] Our results show that the surviving irradiated tumors are more tolerant of unrepaired and misrepaired DNA damage. However, this hypothesis needs to be tested by investigating markers related to genomic instability in tumors. Another finding of our study was the difference in the size of tumor nuclei after radiotherapy. We observed the size of the nuclei increased in irradiated tumors. It has been shown that radiation may induce nuclear abnormalities in tumors, which results in clonogenic cell death.^[52] However, these changes usually occur within a few days after radiation and can lead to delayed cell death. Changes in the nuclei size of the irradiated tumors 11 days after radiotherapy need to be investigated in more detail, but corroborated with the above genomic instability hypothesis.

Finally, we evaluated the response of treated and un-treated breast cancer brain metastases with MRI. We showed all the tumors, whether treated or un-treated, grew at least three times over the duration of 11 days. Moreover, no significant effect was seen between fractional growth of tumors treated with 16 Gy versus 24 Gy as segmented on MRI. The MDA-MB-231-BR cells are known to be edemic lesions. In the bSSFP sequence the edema appears as hyper-intense regions, which have contributed to the tumor volume segmentation. In contrast, histology sections of these tumors showed irradiated tumor clusters are surrounded by pockets of edema, and the tumor cell density decreased significantly with the amount of radiation dose. We also observed that the tumor cell density in the irradiated tumors 11 days after radiotherapy is about half of the un-irradiated side and acute setting. Therefore, edema may mask tumor responses assessed by bssfp MRI as the irradiated tumors grew about 3 times in volume. In some sense, this could be interpreted as pseudoprogession in brain metastases after radiation therapy.^[53] Pseudoprogession is an effect of ionizing radiation, which result in enlarging lesions that mimics the tumor progession but stabilizes over time.^[54]

Furthermore, we employed tumors in un-irradiated side of the mouse brain as the control of the treated side. There was a significant difference between the growth rate of the tumors in the control (0 Gy) group and tumors in the un-irradiated (0* Gy) sides. Monte-Carlo dose simulation for the given treatment plan showed the un-irradiated side received doses up to 1.7 Gy for hemi brain radiation (24 Gy) due to the scatter and beam penumbra. This dose in the range of 1-2 Gy could have a role in the significant differences seen between the growth of control (sham) and un-irradiated tumors. Another possible hypothesis is the radiation-induced bystander effect. This phenomenon is defined as the induction of biological effects in cells that are not directly irradiated but are close to the irradiated ones.^[55] In our study, this effect may have happened between irradiated and un-irradiated tumors in the two hemispheres of the mouse brain.^[56]

One of the limitations of this study was the tumor model itself. The growth of MDA-MB-231-BR tumor is known to be exponential, and in most of the studies the endpoint for this model is less than 30 days after tumor injection.^[57] However, to observe the effect of radiation longitudinally we needed to keep the mice alive until 11 days post-

treatment. This time-point corresponded to day 37 after injection, which is beyond the typical end-point of this tumor model. This factor is the reason for the relatively small size of our longitudinal cohort as we have lost animals before day 37.

3.5 Conclusions

Brain metastasis is a growing problem in breast cancer patients. New treatment strategies for brain metastasis are necessary. Radiotherapy is an established treatment that currently is used to treat a majority of brain metastasis patients. Fundamental radiobiological questions provide and suggest evidence for further improvements and optimization in the clinics. In this study, we evaluated the radiation dose-response of triple-negative breast cancer brain metastases. We found in the acute setting that γ -H2AX in tumors could be saturated at the higher dose level while normal mouse brain tissue continues to increase phosphorylation of H2AX. In the longitudinal setting 11 days after treatment, we found the response of irradiated tumors at both dose levels differed from un-irradiated counterparts in γ -H2AX fluorescence intensity, tumor cell density, and tumor nuclear size. Significant difference was found on MRI between radiated and un-irradiated tumors for the dose of 16 Gy and a trend was seen for the 24 Gy. In addition, significant difference was detected between two radiation doses of 16 and 24 Gy on the DAPI histological quantification but not on MRI analyses. Our results give insight about how triple-negative breast cancer brain metastasis respond to ionizing radiation and sets a platform for further investigations with different cell lines and radiobiological questions.

3.6 Acknowledgment

We would like to thank Carmen Simedrea for cardiac injection and Yuhua Chen for assistance in animal perfusion.

3.7 References

1. Patchell R a. The management of brain metastases. *Cancer Treat Rev* 2003;29(6):533–40.
2. Gavrilovic IT, Posner JB. Brain metastases: Epidemiology and pathophysiology. *J Neurooncol* 2005;75(1):5–14.
3. Davis FG, Dolecek T a, Mccarthy BJ, Villano JL. Toward determining the lifetime occurrence of metastatic brain tumors estimated from 2007 United States cancer incidence data Faith. *Neuro Oncol* 2012;14(9):1171–7.
4. Doh LS, Amato RJ, Paulino AC, Teh BS. Radiation therapy in the management of brain metastases from renal cell carcinoma. *Oncology (Williston Park)* 2006;20(6):603–13; discussion 613, 616, 619–20 passsim.
5. Chambers AF, Groom AC, MacDonald IC. Dissemination and growth of cancer cells in metastatic sites. *Nat Rev Cancer* 2002;2(8):563–72.
6. Nayak L, Lee EQ, Wen PY. Epidemiology of brain metastases. *Curr Oncol Rep* 2012;14(1):48–54.
7. Ranjan T, Abrey LE. Current management of metastatic brain disease. *Neurotherapeutics* 2009;6(3):598–603.
8. Perez CA, Brady LW. Perez and Brady's principles and practice of radiation oncology. 6th ed. Philadelphia: Wolters Kluwer Health/Lippincott Williams & Wilkins; 2013.
9. McTyre E, Scott J, Chinnaiyan P. Whole brain radiotherapy for brain metastasis. *Surg. Neurol. Int.* 2013;4(Suppl 4):S236–44.
10. Khuntia D. Review Article Contemporary Review of the Management of Brain Metastasis with Radiation. *Adv Neurosci* 2015;2015:13.

11. Nieder C, Walter K. Dose / effect relationships for brain metastases. *Survival (Lond)* 1998;346–50.
12. Nieder C, Berberich W, Schnabel K. Tumor-related prognostic factors for remission of brain metastases after radiotherapy. *Int. J. Radiat. Oncol. Biol. Phys.* 1997;39(1):25–30.
13. Son CH, Jimenez R, Niemierko A, Loeffler JS, Oh KS, Shih H a. Outcomes after whole brain reirradiation in patients with brain metastases. *Int J Radiat Oncol Biol Phys* 2012;82(2):167–72.
14. Niikura N, Hayashi N, Masuda N, Takashima S, Nakamura R, Watanabe KI, et al. Treatment outcomes and prognostic factors for patients with brain metastases from breast cancer of each subtype: A multicenter retrospective analysis. *Breast Cancer Res Treat* 2014;147(1):103–12.
15. Nam B-H, Kim SY, Han H-S, Kwon Y, Lee KS, Kim TH, et al. Breast cancer subtypes and survival in patients with brain metastases. *Breast Cancer Res* 2008;10(1am):R20.
16. Kennecke H, Yerushalmi R, Woods R, Cheang MCU, Voduc D, Speers CH, et al. Metastatic behavior of breast cancer subtypes. *J Clin Oncol* 2010;28(20):3271–7.
17. Lin NU, Claus E, Sohl J, Razzak AR, Arnaout A, Winer EP. Sites of Distant Relapse and Clinical Outcomes in Patients with Metastatic Triple-Negative Breast Cancer: High Incidence of Central Nervous System Metastases. 2010;113(10):2638–45.
18. Lockman PR, Mittapalli RK, Taskar KS, Rudraraju V, Bohn K a, Adkins CE, et al. Heterogeneous blood-tumor barrier permeability determines drug efficacy in experimental brain metastases of breast cancer. *Clin Cancer Res* 2011;16(23):5664–78.
19. Sedelnikova O a, Pilch DR. Histone H2AX in DNA Damage and Repair. *Cancer Biol Ther* 2003;(June):233–5.

20. Rogakou EP, Pilch DR, Orr AH, Ivanova VS, Bonner WM. DNA Double-stranded Breaks Induce Histone H2AX Phosphorylation on Serine 139. *J Biol Chem* 1998;273(10):5858–68.
21. Rothkamm K, Horn S. γ -H2AX as protein biomarker for radiation exposure. *Ann Ist Super Sanita* 2009;45(3):265–71.
22. Bonner WM, Redon CE, Dickey JS, Nakamura AJ, Olga A, Solier S, et al. γ H2AX and cancer. *Cancer* 2011;8(12):957–67.
23. Olive L. Endogenous DNA breaks: γ H2AX and the role of telomeres. 2009;1(2):154–6.
24. Sedelnikova O a, Bonner WM. γ H2AX in Cancer Cells ND ES SC RIB. 2006;(December):2909–13.
25. Pouliliou S, Koukourakis MI. Gamma histone 2AX (γ -H2AX)as a predictive tool in radiation oncology. *Biomarkers* 2014;19:167–80.
26. Redon CE, Nakamura AJ, Martin OA, Parekh PR, Weyemi US, Bonner WM. Recent developments in the use of γ -H2AX as a quantitative DNA double-strand break biomarker. 3(2):168–74.
27. Kunwar A, Haston CK. DNA damage at respiratory distress, but not acute time-points, correlates with tissue fibrosis following thoracic radiation exposure in mice. *Int J Radiat Biol* 2015;91(4):360–7.
28. Bhogal N, Kaspler P, Jalali F, Hyrien O, Chen R, Hill RP, et al. Late residual gamma-H2AX foci in murine skin are dose responsive and predict radiosensitivity in vivo. *Radiat Res* 2010;173(1):1–9.
29. Andratschke N, Blau T, Schill S, Nieder C. Late residual γ -H2AX foci in murine spinal cord might facilitate development of response-modifying strategies: A research hypothesis. *Anticancer Res* 2011;31(2):561–4.

30. Yoneda T, Williams PJ, Hiraga T, Niewolna M, Nishimura R. A bone-seeking clone exhibits different biological properties from the MDA-MB-231 parental human breast cancer cells and a brain-seeking clone in vivo and in vitro. *J Bone Miner Res* 2001;16(8):1486–95.
31. Conley F. Development of a metastatic brain tumor model in mice. *Cancer Res* 1979;39(March):1001–7.
32. Perera M, Ribot EJ, Percy DB, McFadden C, Simeanea C, Palmieri D, et al. In Vivo Magnetic Resonance Imaging for Investigating the Development and Distribution of Experimental Brain Metastases due to Breast Cancer. *Transl Oncol* 2012;5(3):217–25.
33. Percy DB, Ribot EJ, Chen Y, McFadden C, Simeanea C, Steeg PS, et al. In Vivo Characterization of Changing Blood-Tumor Barrier Permeability in a Mouse Model of Breast Cancer Metastasis. *Invest Radiol* 2011;46(11):718–25.
34. Scheffler K, Lehnhardt S. Principles and applications of balanced SSFP techniques. *Eur Radiol* 2003;13(11):2409–18.
35. Jensen MD, Hrinivich WT, Jung J a, Holdsworth DW, Drangova M, Chen J, et al. Implementation and commissioning of an integrated micro-CT/RT system with computerized independent jaw collimation. *Med Phys* 2013;40(8):0817061–08170613.
36. Thind K, Jensen MD, Hegarty E, Chen AP, Lim H, Martinez-Santesteban F, et al. Mapping metabolic changes associated with early Radiation Induced Lung Injury post conformal radiotherapy using hyperpolarized ¹³C-pyruvate Magnetic Resonance Spectroscopic Imaging. *Radiother Oncol* 2014;110(2):317–22.
37. Ford EC, Achantac P, Purgerc D, Armoura M, Reyesa J, J. Fonga L, et al. Localized CT-Guided Irradiation Inhibits Neurogenesis in Specific Regions of the Adult Mouse Brain. 2012;175(6):774–83.

38. Ivashkevich A, Redon CE, Nakamura AJ, Martin RF, Martin OA. Use of the γ -H2AX assay to monitor DNA damage and repair in translational cancer research. *Cancer Lett* 2013;487:109–13.
39. Anderson D, Andrais B, Mirzayans R, Siegbahn E a, Fallone BG, Warkentin B. Comparison of two methods for measuring γ -H2AX nuclear fluorescence as a marker of DNA damage in cultured human cells: applications for microbeam radiation therapy. *J Instrum* 2013;8:6008–16.
40. Helen C. Turner, David J. Brenner, Youhua Chen, Antonella Bertucci, Jian Zhang, Hongliang Wang, Oleksandra V. Lyulko, Yanping Xu, Igor Shuryak, Julia Schaefer, Nabil Simaan, Gerhard Randers-Pehrson, Y. Lawrence Yao SAA, Garty G. Adapting the γ -H2AX Assay for Automated Processing in Human Lymphocytes. 1. Technological Aspects. *Radiat Res* 2012;29(6):997–1003.
41. Pereira CF, Terranova R, Ryan NK, Santos J, Morris KJ, Cui W, et al. Heterokaryon-based reprogramming of human B lymphocytes for pluripotency requires Oct4 but not Sox2. *PLoS Genet* 2008;4(9):1–14.
42. Ernst Schmid T, Zlobinskaya O, Multhoff G. Differences in Phosphorylated Histone H2AX Foci Formation and Removal of Cells Exposed to Low and High Linear Energy Transfer Radiation. *Curr Genomics* 2012;13(6):418–25.
43. Yu TY, Chu EHM, Lambur H, Olive PL. Expression of phosphorylated histone H2AX in cultured cell lines following exposure to X-rays. *Int J Radiat Biol* 2003;79(5):351–68.
44. Kotenko K V., Bushmanov AY, Ozerov I V., Guryev D V., Anchishkina N a., Smetanina NM, et al. Changes in the number of double-strand DNA breaks in Chinese hamster V79 cells exposed to γ -radiation with different dose rates. *Int J Mol Sci* 2013;14(7):13719–26.
45. Moiseenko V, Banáth JP, Duzenli C, Olive PL. Effect of prolonging radiation delivery time on retention of gammaH2AX. *Radiat Oncol* 2008;3:18.

46. Löbrich M, Shibata A, Beucher A, Fisher A, Ensminger M, Goodarzi A a., et al. γ H2AX foci analysis for monitoring DNA double-strand break repair: Strengths, limitations and optimization. *Cell Cycle* 2014;9(4):662–9.
47. Kinner A, Wu W, Staudt C, Iliakis G. Gamma-H2AX in recognition and signaling of DNA double-strand breaks in the context of chromatin. *Nucleic Acids Res* 2008;36(17):5678–94.
48. Mariotti LG, Pirovano G, Savage KI, Ghita M, Ottolenghi A, Prise KM, et al. Use of the γ -H2AX assay to investigate DNA repair dynamics following multiple radiation exposures. *PLoS One* 2013;8(11):1–12.
49. Banáth JP, Klokov D, MacPhail SH, Banuelos CA, Olive PL. Residual gammaH2AX foci as an indication of lethal DNA lesions. *BMC Cancer* 2010;10(4):1–12.
50. Nakamura AJ, Redon CE, Bonner WM, Sedelnikova O a. Telomere-dependent and telomere-independent origins of endogenous DNA damage in tumor cells. *Aging (Albany NY)* 2009;1(2):212–8.
51. Yu T, MacPhail SH, Banáth JP, Klokov D, Olive PL. Endogenous expression of phosphorylated histone H2AX in tumors in relation to DNA double-strand breaks and genomic instability. *DNA Repair (Amst)* 2006;5:935–46.
52. Sato N, Mizumoto K, Masafumi N, Tanaka M. Radiation-Induced Centrosome Overduplication and Multiple Mitotic Spindles in Human Tumor Cells. *Exp Cell Res* 2000;326:321–6.
53. Wiggenraad R, Bos P, Verbeek-de Kanter A, Lycklama À Nijeholt G, van Santvoort J, Taphoorn M, et al. Pseudo-progression after stereotactic radiotherapy of brain metastases: lesion analysis using MRI cine-loops. *J Neurooncol* 2014;437–43.
54. Parvez K, Parvez A, Zadeh G. The diagnosis and treatment of pseudoprogression, radiation necrosis and brain tumor recurrence. *Int J Mol Sci* 2014;15(7):11832–46.

55. Hei TK, Zhou H, Ivanov VN, Hong M, Lieberman HB, Amundson SA, et al. Mechanism of radiation-induced bystander effects: a unifying model. 2015;60(8):943–50.
56. Azzam EI, de Toledo SM, Little JB. Stress signaling from irradiated to non-irradiated cells. *Curr Cancer Drug Targets* 2004;4(1):53–64.
57. Perera M, Ribot EJ, Percy DB, Mcfadden C, Simeone C, Palmieri D, et al. In Vivo Magnetic Resonance Imaging for Investigating the Development and Distribution of Experimental Brain Metastases due to Breast Cancer. *Transl Oncol* 2012;5(3):217–25.

Chapter 4

4 Conclusions and Future Directions

This study used a biological marker for DNA double-stranded breaks and noninvasive magnetic resonance imaging to evaluate and characterize the response of breast cancer brain metastases to different radiation doses. To the best of our knowledge, this is the first study to investigate the radiation dose-response in breast cancer brain metastasis model. Custom designed 3D-printed mouse head holder facilitated the irradiation of mouse half brain. This approach gave the advantage of investigating radiation dose-response in half of the brain while using the other half as a control. The work presented in this thesis provides a platform for further research in radiation effects *in-vivo*. The sections below summarize the significant findings in this thesis and future directions that can be followed.

4.1 Chapter 2

4.1.1 3D-Printed Mouse Holder: Summary

The deployment of laboratory findings and their translation into clinical setting is supported by preclinical research. Recently in the field of radiation therapy, the technological disparity between preclinical research and human advanced treatments has decreased with the development of sophisticated small animals irradiators.^[1] Although most of these units are equipped with on-board image guidance to assist with the animal positioning, this capability is not suffice for irradiating sub-regional anatomical parts of the small animals.^[2] The scale of targeting error can be appreciated when one considers that for mouse hemispherical irradiation, we are aiming to irradiate 5 mm of the brain and all structures within that half.

For the radiation dose-response study described in Chapter 3, we designed a mouse head holder for the micro-CT/RT unit. We fabricated our device using 3D-printer and evaluated our actual radiation targeting error in tissue from the intended anatomical

target using immunohistochemistry. The γ -H2AX stain showed that on average our targeting error was less than 0.15 mm. The 3D-printed mouse head holder helped to alleviate the concern of targeting accuracy for our study. Although many small animal fixation devices have been introduced and evaluated by different groups, the unique feature of this device is its design and the method of fabrication.^[2-4] The work presented sets the platform for using 3D-printing technology to build desired experimental devices in a timely and cost-effective manner. In addition, it opens the prospect of sharing and collaboration, as 3D-printers are now widely available.

4.1.2 Future Work

The custom designed head holder is dedicated to mouse irradiation on the micro-CT/RT couch. The present study performed hemi-brain irradiation. A future study can be irradiating individual metastasis as identified with magnetic resonance imaging (MRI). This will require pre-treatment MRI, cone beam CT just prior to radiation, fusion between MRI and cone beam CT to guide beam placement, and irradiation. The design can also be modified for other small animal models such as rats and/or other imaging modalities. For instance, a multi-purpose restrainer can be designed for the rat glioma model^[5] that can serve both as a stereotactic device for tumor implant and as a holder for radiotherapy and imaging.

4.2 Chapter 3

4.2.1 Acute Radiation Dose-Response Study: Summary

For the acute radiation dose-response study, mice were sacrificed 30 minutes after various radiation doses. We employed γ -H2AX, as a marker that reflects the radiation-induced DNA double-stranded breaks.^[6] The results showed γ -H2AX fluorescence intensity in breast cancer brain metastases does not increase linearly with radiation dose and, in fact, decreases at 24 Gy. In contrast, mouse normal brain cells showed a linear trend between γ -H2AX fluorescence intensity and radiation dose. This finding generates

new questions related to damage and repair signaling in tumors versus normal brain tissues.

4.2.2 Acute Radiation Dose-Response Study: Future Work

We hypothesized that the saturation of γ -H2AX to radiation dose in the acute study in MDA-MB-231-BR tumor model could be due to either the low dose-rate of our unit or the γ -H2AX marker itself. To verify if it is the effect of dose-rate, one can irradiate the whole brain of the same animal model with other irradiator units such as Co⁶⁰ and compare the induced γ -H2AX fluorescence intensity with what we have presented. Moreover, tumors and normal brain tissues can be immune-stained for other ionizing radiation-induced foci (IRIF) markers that are involved in DNA repair and DNA damage signaling. Co-localization of γ -H2AX foci with tumor suppressor TP53 binding protein 1 (53BP1) and/or Mre11 can be investigated.^[7,8]

4.2.3 *Ex-Vivo* Longitudinal Radiation Dose-Response Study: Summary

To investigate the radiation dose-response longitudinally after treatment, mice were sacrificed 11 days after receiving half-brain radiation therapy. The histological sections were stained for γ -H2AX to assess the residual amount of damage induced. The results suggested:

- 1) Even after normalizing γ -H2AX by the area of nucleus, tumors that survived 11 days after RT had significantly higher γ -H2AX intensity (Fig. 3-8) than the un-irradiated and control tumors
- 2) Irradiated tumors had larger nuclei compared to the un-irradiated and control tumors
- 3) The amount of γ -H2AX returned to baseline level for normal brain nuclei

4.2.4 *Ex-Vivo* Longitudinal Radiation Dose-Response Study: Future Work

To the best of our knowledge, there is no clear reason why irradiated tumors retained higher amount of γ -H2AX 11 days after radiotherapy. Our primary speculation is the remaining surviving irradiated tumors are more genomic unstable compared to un-irradiated ones. As for their large nuclei, one reason can be due to the chromosome segregation error during mitosis that resulted in aneuploidy. Staining for markers such as γ -tubulin would evaluate centrosome amplification and aneuploidy in irradiated tumors.^[9,10]

Another interesting approach can be related to the chromatin structure and its architecture in the tumors after radiation. It has been shown that the structure of the chromatin plays a pivotal role in DNA DSBs repair. Chromatin global relaxation happens as early as 1 hour post-radiation to facilitate the repair mechanism.^[11,12] The question remains how this structure changes acutely in tumors after various doses of radiation and if they also preserve their relaxed structure 11 days after radiotherapy. One of the markers for the relaxed chromatin (euchromatin) state is acetylated histone 3 (H3). Interesting, enhanced γ -H2AX foci have been correlated with abundant chromatin-remodeling and histone hyperacetylation.^[13] More investigation in this matter may be beneficial for understanding the tumor recurrence after initial radiation therapy in patients diagnosed with brain metastasis.^[14]

4.2.5 *In-Vivo* Longitudinal Radiation Dose-Response Study: Summary

For the *in-vivo* radiation dose-response study, mice were imaged with MRI bSSFP sequence before and 11 days after treatment. The effect of radiation on the growth of tumors was significantly different between treated and un-treated side for 16 Gy; however, no significant difference was detected between two radiation doses of 16 and 24 Gy and 24 Gy and its contralateral part. In contrast, histological DAPI tumor cell density showed significant difference between these two radiation doses.

4.2.6 *In-Vivo* Longitudinal Radiation Dose-Response Study: Future work

In the clinical setting, MRI is the gold standard imaging technique for patient follow-up after treatment. Depending on the MRI sequence used, edemic parts of the tumors can be misinterpreted to be positive lesions. The bSSFP sequence detects brain metastases regardless of their permeability; however, this sequence also shows the fluidity in the tumors as positive regions that can contribute to tumor segmentation and volume.^[15] Other MRI sequences such as diffusion-weighted imaging (DWI) can be used. (Figure 4-1) The extracellular water molecules will have enhanced diffusion when the tumor cell density decreases due to treatment, making this an interesting imaging marker to assess radiation response.

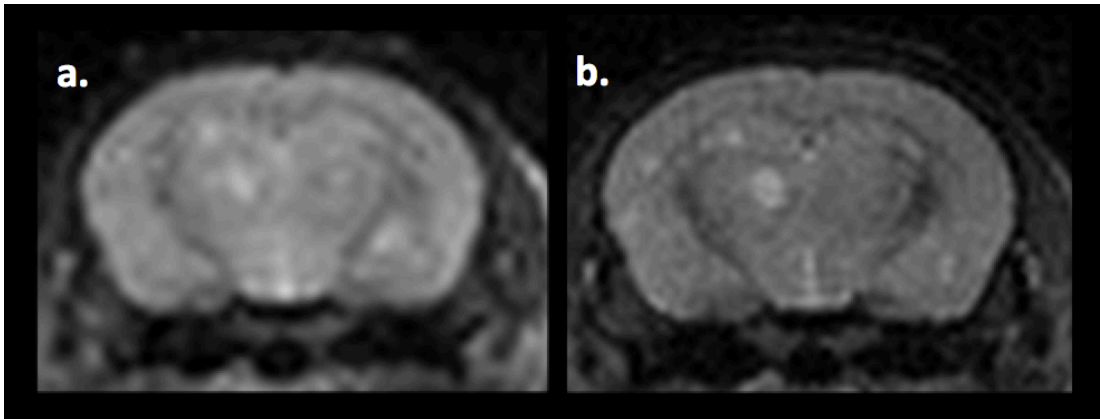


Figure 4-1: Mouse brain tumor model imaged with DWI sequence on 9.4T scanner. Images from two different b-values are shown. (a=500 s/mm², b=1000 s/mm²)

4.3 References

1. Butterworth KT, Prise KM, Verhaegen F. Small animal image-guided radiotherapy: status, considerations and potential for translational impact. *Br J Radiol* 2015;88(1045):20140634.
2. Armour M, Ford E, Iordachita I, Wong J. CT Guidance is Needed to Achieve Reproducible Positioning of the Mouse Head for Repeat Precision Cranial Irradiation. *Radiation Res* 2010;173(1):119–23.
3. Kiehl EL, Stojadinovic S, Malinowski KT, Limbrick D, Jost SC, Garbow JR, et al. Feasibility of small animal cranial irradiation with the microRT system. *Med Phys* 2008;35(10):4735–43.
4. Baumann BC, Benci JL, Santoiemma PP, Chandrasekaran S, Hollander AB, Kao GD, et al. An Integrated Method for Reproducible and Accurate Image-Guided Stereotactic Cranial Irradiation of Brain Tumors Using the Small Animal Radiation Research Platform. *Transl Oncol* 2012;5(4):230–7.
5. Badie B, Hunt K, Economou J, Black K. Stereotactic delivery of a recombinant adenovirus into a C6 glioma cell line in a rat brain tumor model. *Neurosurgery* 1994;35(5):910–5.
6. Sharma A, Singh K, Almasan A. Histone H2AX phosphorylation: A marker for DNA damage. *Methods Mol Biol* 2012;920:613–26.
7. Marková E, Schultz N, Belyaev IY. Kinetics and dose-response of residual 53BP1/gamma-H2AX foci: co-localization, relationship with DSB repair and clonogenic survival. *Int J Radiat Biol* 2007;83(5):319–29.
8. Furuta T, Takemura H, Liao ZY, Aune GJ, Redon C, Sedelnikova O a., et al. Phosphorylation of histone H2AX and activation of Mre11, Rad50, and Nbs1 in response to replication-dependent DNA double-strand breaks induced by mammalian DNA topoisomerase I cleavage complexes. *J Biol Chem* 2003;278(22):20303–12.

9. Fukasawa K. Centrosome amplification, chromosome instability and cancer development. *Cancer Lett* 2005;230(1):6–19.
10. Sato N, Mizumoto K, Masafumi N, Tanaka M. Radiation-Induced Centrosome Overduplication and Multiple Mitotic Spindles in Human Tumor Cells. *Exp Cell Res* 2000;326:321–6.
11. Mariotti LG, Pirovano G, Savage KI, Ghita M, Ottolenghi A, Prise KM, et al. Use of the γ -H2AX assay to investigate DNA repair dynamics following multiple radiation exposures. *PLoS One* 2013;8(11):1–12.
12. Cowell IG, Sunter NJ, Singh PB, Austin C a., Durkacz BW, Tilby MJ. γ -H2AX foci form preferentially in euchromatin after ionising-radiation. *PLoS One* 2007;2(10):1–8.
13. Banáth JP, Bañuelos C a., Klovov D, MacPhail SM, Lansdorp PM, Olive PL. Explanation for excessive DNA single-strand breaks and endogenous repair foci in pluripotent mouse embryonic stem cells. *Exp Cell Res* 2009;315(8):1505–20.
14. Shinoura N, Yamada R, Okamoto K, Nakamura O, Shitara N. Local recurrence of metastatic brain tumor after stereotactic radiosurgery or surgery plus radiation. *J Neurooncol* 2002;60(1):71–7.
15. Perera M, Ribot EJ, Percy DB, Mcfadden C, Simedrea C, Palmieri D, et al. In Vivo Magnetic Resonance Imaging for Investigating the Development and Distribution of Experimental Brain Metastases due to Breast Cancer. *Transl Oncol* 2012;5(3):217–25.

Appendices

Appendix A: Animal Use Protocol

Page 1 of 1

>>> eSiriusWebServer <[REDACTED]> 2014/11/05 11:32 AM >>>



2009-080::5:

AUP Number: 2009-080

AUP Title: Non-Invasive Imaging of Metastasis: Detection, Monitoring and Intervention

Yearly Renewal Date: 11/01/2014

The YEARLY RENEWAL to Animal Use Protocol (AUP) 2009-080 has been approved, and will be approved for one year following the above review date.

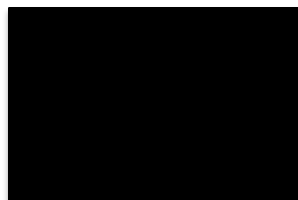
1. This AUP number must be indicated when ordering animals for this project.
2. Animals for other projects may not be ordered under this AUP number.
3. Purchases of animals other than through this system must be cleared through the ACVS office. Health certificates will be required.

REQUIREMENTS/COMMENTS

Please ensure that individual(s) performing procedures on live animals, as described in this protocol, are familiar with the contents of this document.

The holder of this Animal Use Protocol is responsible to ensure that all associated safety components (biosafety, radiation safety, general laboratory safety) comply with institutional safety standards and have received all necessary approvals. Please consult directly with your institutional safety officers.

Submitted by: Kinchlea, Will D
on behalf of the Animal Use Subcommittee



This information is directed in confidence solely to the person named above and may contain confidential and/or privileged material. This information may not otherwise be distributed, copied or disclosed. If you have received this e-mail in error, please notify the sender immediately via a return e-mail and destroy original message. Thank you for your cooperation.

Appendix B: Fluorescent γ -H2AX Immunohistochemistry Standard Operating Procedure on Mouse Frozen Sections

****Everything at room temperature unless otherwise specified****

- 1) Antigen retrieval: Use 10mMol sodium citrate pH 6.0. Put the slides in a jar and pour 10 mMol Na citrate. Put the jar with slides in the microwave. Set the power to 10 and watch until it boils. Then set the microwave power to 1 and set the timer for 10 minutes. Wait 30 minutes so that the slides get to room temperature.
- 2) Wash: 3 x 5 min PBS. Draw around each section with gnomer pen (hydrophobic pen).
- 3) Blocking: 10% goat serum + 0.3% Triton + PBS: Apply blocking buffer and leave for 1 hour in the humid chamber.
- 4) Primary Antibody: Primary antibody is Millipore Anti-phospho-Histone H2AX mouse (clone JBW301). The dilution is 1:700 in blocking buffer. For negative control do not apply primary. Put the sections in the humid chamber and fridge (4°C) overnight.
- 5) Wash: 3 x 5 min in PBS.
- 6) Secondary Antibody: Alexa Fluor® 594 Goat Anti-Mouse IgG. Dilution is 1:500. Rinse the slides and put the secondary. Put the slides in dark (heavy duty foil) for 1hour.
- 7) Wash: 3 x 5 min in PBS.
- 8) Counterstaining: Dry the slides and put 3 drops of DAPI Vectashield on cover glass and flip the slides. Use nail polish to seal them and let them dry.

Appendix C: License and Permission Usage

Nature Publishing Group License – Chapter 1

NATURE PUBLISHING GROUP LICENSE TERMS AND CONDITIONS

Jun 29, 2015

This is a License Agreement between Niloufar Zarghami ("You") and Nature Publishing Group ("Nature Publishing Group") provided by Copyright Clearance Center ("CCC"). The license consists of your order details, the terms and conditions provided by Nature Publishing Group, and the payment terms and conditions.

All payments must be made in full to CCC. For payment instructions, please see information listed at the bottom of this form.

License Number	3658370457437
License date	Jun 29, 2015
Licensed content publisher	Nature Publishing Group
Licensed content publication	Nature Reviews Cancer
Licensed content title	Metastasis: from dissemination to organ-specific colonization
Licensed content author	Don X. Nguyen, Paula D. Bos, Joan Massagué
Licensed content date	Apr 1, 2009
Volume number	9
Issue number	4
Type of Use	reuse in a dissertation / thesis
Requestor type	academic/educational
Format	print and electronic
Portion	figures/tables/illustrations
Number of figures/tables/illustrations	1
High-res required	no
Figures	Figure-2
Author of this NPG article	no
Your reference number	None
Title of your thesis / dissertation	Evaluation of Radiation-Induced DNA Double-Stranded Breaks and Tumor Response in a Breast Cancer Brain Metastasis Model
Expected completion date	Aug 2015
Estimated size (number of pages)	100

Curriculum Vitae

Name: Niloufar Zarghami

Post-secondary Education and Degrees: The University of Western Ontario
London, Ontario, Canada
2013-2015 MSc. Medical Biophysics

Shahid Beheshti University of Medical Sciences
Tehran, Iran
2008-2012 BSc. Radiation Therapy

Honours and Awards: Pamela Greenaway-Kohlmeier Translational Breast Cancer Unit
2013-2015

Province of Ontario Graduate Scholarship
2014-2015

The 11th Annual Oncology Research & Education Poster Award
2014

Western Graduate Scholarship
2013-2015

Academic Excellence Award, Shahid Beheshti University
2010, 2011

Appreciation Certificate, Shahid Beheshti University
2008, 2009

Shahid Beheshti Undergraduate Scholarship
2008-2012

Related Work Experience Undergraduate Research Assistant
Shahid Beheshti University of Medical Sciences
2011-2012

Undergraduate Teacher Assistant
Shahid Beheshti University of Medical Sciences
2010-2011

Radiation Therapy Technologist
Behnam Daheshpour Cancer Institute
2011-2012

Publications:

Journal Articles:

- **Zarghami. N**, Jensen. M, Talluri. S, Foster. P, Chambers. A, Dick. F, Wong. E “Immunohistochemical evaluation of mouse brain irradiation targeting accuracy with 3D-printed immobilization device”, Journal of Medical Physics, Under-revision *Journal of Medical Physics*
- **Zarghami. N**, Murrell D, Jensen. M, Dick. F, Chambers. A, Foster. P, Wong. E “Evaluation of inherent and residual radiation-induced DNA double-stranded breaks and tumour response in a breast cancer brain metastasis model”, [In preparation]

Accepted Conference Proceeding Abstracts:

- **Zarghami. N**, Murrell. D, Jensen. M, Dick. F, Chambers. A, Foster. P, Wong. E “ Quantitative evaluation of inherent and radiation-induced DNA double-stranded breaks and tumor response in breast cancer brain metastasis model”, London Oncology Research & Education day, 2015, Poster
- Murrell. D, **Zarghami. N**, Jensen. M, Chambers. A, Wong. E, Foster. P. “Longitudinal MRI evaluation of whole brain radiotherapy on brain metastasis development and dormancy in a mouse model”, IUPESM World Congress, Toronto, Canada, 2015, Oral
- **Zarghami. N**, Jensen. M, Chambers. A, Foster. P, Wong. E, “Histological evaluation of targeting accuracy of 3D-printed immobilization device for mouse brain irradiation”, 2nd Symposium on small animal precision image guided radiation therapy, Vancouver, Canada, August 2014, Oral
- **Zarghami. N**, Jensen. M, Chambers. A, Foster. P, Wong. E “Histological evaluation of targeting accuracy of 3D-printed immobilization device for mouse brain irradiation”, London Oncology Research & Education day, 2014, Poster
- Murrell. D, Hamilton. A, Jensen. M, **Zarghami. N**, Chambers. A, Wong. E, Foster. P, “MRI Characterization of the Responses of Brain Metastatic Breast Cancer Cells to Whole Brain Micro-irradiation in Mice”, World Molecular Imaging Symposium, 2013, Poster